Control of 3' splice site selection by the yeast splicing factor Fyv6

Katherine A. Senn[1]*, Karli A. Lipinski[2]*, Natalie J. Zeps[1], Amory F. Griffin[1],

Max E. Wilkinson[3, 4], Aaron A. Hoskins[1,2]

*indicates co-first authors

[1] Department of Biochemistry, University of Wisconsin-Madison, Madison, WI 53706 USA

[2] Department of Chemistry, University of Wisconsin-Madison, Madison, WI 53706 USA

[3] MRC Laboratory of Molecular Biology, Cambridge CB2 0QH UK

[4]Present Addresses: Broad Institute of MIT and Harvard, Cambridge MA 02142 USA and McGovern Institute for Brain Research, Massachusetts Institute of Technology, Cambridge, MA 02139 USA

CORRESPONDING AUTHORS:

Aaron A. Hoskins, ahoskins@wisc.edu

Max E. Wilkinson, mwilkin@mit.edu

RUNNING TITLE: Structure and Function of the Splicing Factor Fyv6

KEYWORDS: yeast, spliceosome, pre-mRNA splicing, cryo-EM, snRNA, snRNP, structure, RNA-Seq

ABSTRACT

Pre-mRNA splicing is catalyzed in two steps: 5' splice site (SS) cleavage and exon ligation. A number of proteins transiently associate with spliceosomes to specifically impact these steps (1st and 2nd step factors). We recently identified Fyv6 (FAM192A in humans) as a 2nd step factor in *S. cerevisiae*; however, we did not determine how widespread Fyv6's impact is on the transcriptome. To answer this question, we have used RNA-seq to analyze changes in splicing. These results show that loss of Fyv6 results in activation of non-consensus, branch point (BP) proximal 3' SS transcriptome-wide. To identify the molecular basis of these observations, we determined a high-resolution cryo-EM structure of a yeast product complex spliceosome containing Fyv6 at 2.3 Å. The structure reveals that Fyv6 is the only 2nd step factor that contacts the Prp22 ATPase and that Fyv6 binding is mutually exclusive with that of the 1st step factor Yju2. We then use this structure to dissect Fyv6 functional domains and interpret results of a genetic screen for *fyv6Δ* suppressor mutations. The combined transcriptomic, structural, and genetic studies allow us to propose a model in which Yju2/Fyv6 exchange facilitates exon ligation and Fyv6 promotes usage of consensus, BP distal 3' SS.

INTRODUCTION

Precursor messenger RNA (pre-mRNA) splicing is catalyzed by a large macromolecular complex called the spliceosome. Spliceosomes are composed of 5 small nuclear ribonucleoproteins (snRNPs), each composed of a small nuclear RNA (snRNA; U1, U2, U4, U5, and U6) and several different protein splicing factors. The snRNPs and dozens of other proteins assemble *de novo* at each intron to form spliceosomes. Spliceosomes are highly dynamic and form different complexes as proteins and snRNAs join and leave. Many of these complexes have been characterized biochemically, genetically, and by cryo-electron microscopy (cryo-EM) (Plaschka et al., 2019). The splicing reaction itself is carried out in two sequential transesterification reactions (**Figure 1A**). First, the 5' splice site (5' SS) is cleaved during formation of an intron lariat (1st step). Second, the intron lariat is removed simultaneously with exon ligation at the 3' SS (2nd step).

The integrity of the genetic information contained within a pre-mRNA depends on correct identification of the 5' and 3' SS by the splicing machinery since a single nucleotide shift in either site could destroy a protein reading frame. In yeast, several DExD/H-box ATPases function to limit usage of suboptimal SS by enhancing splicing fidelity (Chung et al., 2023; Semlow and Staley, 2012). Two of these ATPases, Prp16 and Prp22, impact the fidelity of the 1st and 2nd catalytic steps, respectively. In addition to these roles, Prp16 is also required for remodeling of the spliceosome to permit the 1st-to-2nd step transition (Schwer and Guthrie, 1992), and Prp22 is essential for releasing the mRNA product (Company et al., 1991). While Prp16 does not need to be present during the 1st step (Chung et al., 2023), Prp22 is required to be present for exon ligation if the branch point (BP) to 3' SS distance is $\geq$ 21 nucleotides (nt) (Schwer and Gross, 1998). Despite many biochemical, single molecule, and structural studies, how spliceosomes promote usage of BP distal, Prp22-dependent 3' SS has remained elusive.

Identification of the correct 3' SS is an especially challenging problem given that the consensus sequence in *Saccharomyces cerevisiae* (yeast) and humans is just three nucleotides

62 (YAG, Y=U or C). Cryo-EM structures of spliceosome product (P) complexes have revealed how
63 these nucleotides can be recognized within the spliceosome active site (Bai et al., 2017; Fica et
64 al., 2019; S. Liu et al., 2017; Wilkinson et al., 2017; Zhang et al., 2019). The AG 3' SS dinucleotide
65 is recognized by formation of non-Watson Crick base-pairing interactions with the 5' SS +1G and
66 BP adenosine, while the pyrimidine at the -3 position of the 3' SS is recognized by the Prp8
67 protein. Given this short consensus sequence, multiple different splicing factors also help to
68 ensure that the correct 3' SS is utilized, including Cwc21 and the 2nd step factors Slu7, Prp18, and
69 Prp22 (Crotti et al., 2007; Frank and Guthrie, 1992; Gautam et al., 2015; Kawashima et al., 2014;
70 Roy et al., 2023; Semlow et al., 2016). It is believed that Slu7 and Prp18 help to stabilize 3' SS
71 docking to the active site and that this contributes to 2nd step efficiency. It has been proposed that
72 Prp22 antagonizes 3' SS docking to permit sampling of different 3' SS to ensure that optimal
73 sequences are used as a proofreading mechanism (Mayas et al., 2006; Semlow et al., 2016).
74 Importantly, identification of the correct 3' SS depends not just on identification of the YAG
75 sequence but also involves choosing which YAG sequence to use. Prp18 appears to aid in
76 selection of BP distal 3' SS and avoidance of BP proximal (and often non-consensus) 3' SS. This
77 observation could be due to Prp18 imposing a BP to 3' SS distance constraint, enforcing use of
78 canonical YAG 3' SS sequences, or a combination of the two activities.

79 Recently, Fyv6 was identified as a novel 2nd step factor in yeast (Lipinski et al., 2023).
80 Fyv6 is a homolog of the human protein FAM192A, which was identified in pre-C* structures of
81 the human spliceosome (Zhan et al., 2022). While the impact of FAM192A on human spliceosome
82 activity has not yet been well-characterized, loss of Fyv6 in yeast decreases 2nd step splicing
83 efficiency *in vitro* and results in use of an alternative 3' SS in the *SUS1* pre-mRNA *in vivo*. It is
84 likely that unassigned cryo-EM densities in yeast C* (just prior to exon ligation) and P complexes
85 correspond to Fyv6 since these densities are in analogous locations to that for FAM192A in the
86 human pre-C* structure (Zhan et al., 2022). However, the resolutions of the yeast C* and P

87 complex structures make unambiguous assignment of Fyv6 amino acid side chains and
88 interactions difficult.

89 Here, we use a combination of transcriptomic, structural, biochemical, and genetic assays
90 to elucidate how Fyv6 controls 3' SS usage in yeast. RNA-seq analysis reveals widespread
91 activation of alternative, BP proximal nonconsensus 3' SS in the absence of Fyv6 consistent with
92 biochemical assays that show Fyv6 facilitates splicing of 3' SS located $\geq$ 21 nt from the BP. To
93 further elucidate Fyv6 function, we determined a 2.3 Å cryo-EM structure of the yeast P complex
94 spliceosome in which Fyv6 can be modeled. The structure reveals interactions between Fyv6 and
95 Prp22 as well as a domain in Syf1 that interacts with either Fyv6 or the 1st step factor Yju2. 3D
96 classification allowed us to identify two additional conformational states of P complex and
97 provides insights into the coupling of 3' SS active site docking and the presence of 2nd step factors.
98 We then used this structural data to dissect the functional domains of Fyv6, interpret the results
99 of a genetic screen for suppressors of *fyv6Δ*, and to probe Fyv6 and Prp22 interactions.
100 Combined, we propose a model in which Fyv6 is recruited to the spliceosome via interactions with
101 the NTC component Syf1 in order to promote usage of BP distal, and Prp22-dependent, 3' SS.

102 **RESULTS**

103 **Deletion of *FYV6* Results in Widespread Use of Alternative 3′ Splice Sites**

104 Our previous work showed that loss of *FYV6* causes changes in 3' SS usage in the *SUS1*
105 pre-mRNA. To probe for changes transcriptome-wide, we used nonsense mediated decay (NMD)-
106 deficient (*upf1Δ*, WT) yeast cells expressing or lacking Fyv6. By suppressing NMD, we hoped to
107 limit degradation of alternatively spliced mRNA isoforms generated in the absence of Fyv6
108 (Sayani et al., 2008). Consistent with results from *fyv6Δ* strains, the *fyv6Δ upf1Δ* double mutant
109 strain also showed reduced growth at 30°C and cold-sensitive (*cs*) and temperature-sensitive (*ts*)
110 phenotypes relative to a *upf1Δ* control strain (**Figure 1B**). We then used RNA-Seq to analyze the
111 isolated RNAs from these strains. As expected, many more changes in splicing were observed in

112 the *fyv6Δ upf1Δ* strain relative to the *fyv6Δ* strain (**Figure 1-figure supplement 1A, 1B;**
113 **supplementary tables 1, 2**). This is consistent with many mRNA isoforms generated due to loss
114 of Fyv6 being substrates for NMD. Loss of Fyv6 resulted in a number of changes in gene
115 expression with many non-intron containing genes also being up- or down-regulated (**Figure 1-**
116 **figure supplement 1C**).

117 We compared and classified changes in splicing between strains containing or lacking
118 *FYV6* under permissive growth conditions (30°C) or after the yeast had been shifted to a non-
119 permissive temperature (16 or 37°C) for 1 h (**Figure 1C**). In this case, we only considered events
120 resulting in at least a 10% change in the percent spliced in (PSI) value when *FYV6* is deleted. At
121 all temperatures, we see changes in alternative 3' SS usage in the *fyv6Δ* strain relative to the
122 *FYV6* background. For example, we detected use of the alternative 3' SS in the first intron of the
123 *SUS1* transcript as we previously reported (**Figure 1-figure supplement 1D**; Lipinski et al.,
124 2023). We also saw increased use of a cryptic, nonconsensus GAG 3' SS in the first, but not
125 second, intron of the *YOS1* transcript in the *fyv6Δ* data sets and confirmed this result by RT-PCR
126 (**Figure 1-figure supplement 1E, F**). We observed several cases of alternative 5' SS. However,
127 the majority of these alternative 5' SS were used with equal efficiencies in the WT and
128 *fyv6Δ* strains (**Figure 1-figure supplement 1G**).

129 The strains temperature shifted to 16°C had the largest number of changes due to *FYV6*
130 deletion and the strains shifted to 37°C the least. The temperature shift to 16° caused an increase
131 in the numbers of both alternative 3' SS and retained intron events detected (**Figure 1C**). The
132 changes in alternative 3' SS used at each temperature were mostly unique with few events
133 detected under all three conditions (**Figure 1D**). Collectively, we observed that 61 different RNAs
134 (~20% of introns) changed splicing patterns due to loss of Fyv6. For many of these mRNAs, we
135 detected multiple different 3' SS being used.

136 To investigate these splicing events more closely, we analyzed changes in usage of
137 alterative splice junctions by calculating the Fraction of Annotated Splicing (FAnS) in the presence
138 and absence of Fyv6 (Roy et al., 2023). FAnS ratios report the relative abundance of an alternative
139 splicing event in relation to the main spliced isoform. We calculated FAnS values for all exon
140 junction reads corresponding to usage of a canonical 5' SS and an alternative 3' SS for WT and
141 *fyv6Δ* strains at each temperature. We then calculated the ratios of the *fyv6Δ*/WT FAnS values
142 for each transcript. These results confirm changes in alternative 3' SS usage for both ribosomal
143 protein gene (RPG) and non-RPG transcripts at all conditions (**Figure 1E**). We could not detect
144 any significant differences between RPG and non-RPG splicing with this analysis, suggesting that
145 differences in gene expression and splicing efficiencies between these two classes are not
146 correlated with alternative 3' SS usage. Combined these results show that Fyv6 plays a critical
147 role in defining mRNA isoform production in yeast, particularly under non-optimal growth
148 conditions such as temperature stress.

149 **Fyv6 Facilitates Usage of Branch Point Distal 3′ Splice Sites**

150 We next analyzed the features of the 3' SS impacted by Fyv6 loss. We used RNAs
151 collected from yeast grown at 30°C and sequenced the libraries at higher depth than those used
152 for the temperature-shift experiment described in **Figure 1** (~400 million vs. 200 million reads;
153 **supplementary table 2**). We first identified alternative 3' SS used in each strain, annotated each
154 as being upstream (5') or downstream (3') of the canonical 3' SS (Grate and Ares, 2002), and
155 then calculated the FAnS ratio for each site. This analysis shows that the majority of the alternative
156 3' SS arising from Fyv6 deletion are upstream (**Figure 2A**, pink points above the diagonal). When
157 these alternative 3' SS are mapped according to their nucleotide distance from the canonical site,
158 most of these are found within ~40 nt upstream (**Figure 2B**, purple violin). Plotting these
159 alternative 3' SS sites relative to their distance from the annotated BP reveals that the highest
160 density of sites is $\leq$ 20 nt from the BP for transcripts with the highest FAnS ratios (**Figure 2C**,
161 purple violin). It is important to note that we did not map BP in Fyv6 deletion strains, and it is

162 possible that in some cases a shift in 3' SS usage could also coincide with a shift in the BP. Indeed,
163 a small number of alternative 3' SS detected in the Fyv6 data sets are located upstream of the
164 annotated BP, suggesting activation of an alternative BP and 3' SS. However, we believe that the
165 changes are predominantly due to usage of alternative 3' SS located between the annotated BP
166 and canonical 3' SS.

167 The above results suggest that Fyv6 is important for splicing of 3' SS located distant from
168 the BP. To test this directly and systematically, we created a series of ACT1-CUP1 reporters with
169 various BP to 3' SS distances (9-50 nt, **Figure 2D**, **supplementary table 3**) based on sequences
170 used in previous studies of 3' SS selection (Brys and Schwer, 1996; Frank and Guthrie, 1992;
171 Schwer and Gross, 1998). We transformed strains containing or lacking Fyv6 and without
172 debranchase (Dbr1) to limit degradation of lariat intermediates. We then detected RNA products
173 by primer extension and calculated the 2nd step (exon ligation) efficiency for each reporter (**Figure**
174 **2E, F**). While loss of Fyv6 has minimal impact on exon ligation when BP to 3' SS distances are
175 short (9-15 nt), exon ligation efficiency decreases significantly at distances of 21 nt or greater. In
176 addition, we do not see evidence of cryptic BP usage in these assays. This result is consistent
177 with the RNA-seq analysis and supports a function for Fyv6 in facilitating splicing at BP distal 3'
178 SS.

179 Finally, we analyzed the sequence features of the alternative 3' SS with increased use
180 after loss of Fyv6 (**Figure 2G, H**). For sites located upstream of the canonical 3' SS, we observed
181 much greater sequence variability relative to the canonical site. We detected increased use of
182 highly variable 3' SS including those with atypical HAU (H=A,C,U) and BG (B=C,U,G) motifs and
183 confirmed generation of new RNA isoforms for several of these by RT-PCR (**Figure 2H, figure 2-**
184 **figure supplement 1**). Increased use of variable 3' SS was also observed when the 2nd step
185 factor *PRP18* was deleted (Roy et al., 2023). However, the subset of RNAs most impacted by
186 splicing factor deletion appear to be different. For example, we were not able to detect changes
187 in 3' SS usage for the *UBC12*, *MAF1*, *MUD1*, *PHO85*, *SPT14*, or *YCL002C* transcripts in the *fyv6*Δ

188 data sets as was reported for *prp18*Δ (not shown). Prp18 and Fyv6 likely have transcript-specific
189 effects on splicing outcomes. Combined our results strongly support Fyv6 as a 2nd step splicing
190 factor that facilitates usage of consensus sites located distal to the BP *in vivo*.

191 **A High-Resolution Spliceosome Structure Reveals Fyv6 Interactions**

192 Previous structures of the yeast P-complex spliceosome were solved with resolutions at
193 the core ranging from 3.3 Å to 3.7 Å (Bai et al., 2017; S. Liu et al., 2017; Wilkinson et al., 2017),
194 and with peripheral components such as the Prp22 helicase, U2 snRNP, and Prp19 Complex
195 (NTC) at much lower resolutions (5-10 Å) that precluded detailed investigation. To improve the
196 resolution, we purified P complex as previously described by stalling spliceosome disassembly
197 with a dominant negative mutant of Prp22 (S635A) defective in mRNA release (Schwer and
198 Meszaros, 2000; Wilkinson et al., 2017). However, by collecting a much larger cryo-EM dataset
199 on a more modern electron detector, we were able to resolve the structure to 2.3 Å within the
200 catalytic core, as well as visualize peripheral components at resolutions from 3.0 Å – 3.7 Å (**Figure
201 3A, B; figure 3-figure supplements 1-4; supplementary table 4**). This is the highest resolution
202 spliceosome structure to date. The high-quality density at the active site shows the positions of
203 bases unambiguously, confirming the manner of the non-Watson-Crick base pairing that mediates
204 3' SS recognition (S. Liu et al., 2017; Wilkinson et al., 2017). Monovalent ions bound at the active
205 site were previously shown to be important during the 1st step of splicing (Wilkinson et al., 2021),
206 and our data indicate that the positions of these ions are preserved after exon ligation. Additionally,
207 the density also shows a metal ion, likely potassium, that bridges the base pair between +1G of
208 the 5' SS and -1G of the 3' SS (**Figure 3C**).

209 The 2nd-step splicing factor Prp22 is resolved at 3.0 Å resolution, allowing atomic
210 interpretation for the first time (**Figure 3B** and later figures). Bases 13 – 21 of the 3' exon are
211 visible between the two RecA domains of Prp22 consistent with biochemical footprinting data
212 (Schwer, 2008) (**figure 3-figure supplement 4**). The S635A mutation used to stall P complex is
213 also visible; however, the origin of defective mRNA release due to this mutation is not apparent

214 (Schwer and Meszaros, 2000). The loop containing S635A is in a similar conformation in this
215 structure and in the structure of WT human Prp22 (Felisberto-Rodrigues et al., 2019) (**figure 3-**
216 **figure supplement 4**). Part of the extensive N-terminal domain of Prp22 is resolved and
217 constitutes a long helix that bridges between the Prp22 RecA2 domain and the C-terminal domain
218 of Cwc22; this helix was unassigned in previous P-complex structures (**Figure 4B**).

219 To improve the resolution of the peripheral, flexible regions, we used a new data-driven
220 regularization strategy (Kimanius et al., 2024) that allows focused refinements of much smaller
221 domains than previously possible (**figure 3-figure supplement 2, 4**). Combined with AlphaFold2-
222 assisted modelling, we were able to obtain more accurate models for the U2 snRNP, NTC, U5
223 Sm ring, and Cwc22 N-terminal domains. Our model for the NTC within the P complex is similar
224 to our previous model for the NTC within C and C^i complexes (Wilkinson et al., 2021) (**Figure**
225 **4C**). Notably however, we observed a star-shaped density coordinated by several conserved
226 lysines from Clf1 and Ntc20, which we were able to model as inositol hexakisphosphate (IP_6)
227 (**Figure 4D**). The same density, at lower resolution, is visible in the C complex (Wilkinson et al.,
228 2021). A distinct, separate IP_6 molecule had previously been observed within all catalytic
229 spliceosomes between the B^{act} and P-complex stages coordinated by Prp8 and (for C* and P-
230 complexes) Slu7 (**figure 3-figure supplement 4**). We do not believe that the NTC-bound IP_6 is
231 essential for splicing since deletion of the Clf1 tetratricopeptide repeat that coordinates IP_6 does
232 not result in growth or splicing phenotypes in yeast and Ntc20 is a non-essential splicing factor
233 (Chen et al., 2001; Chung et al., 1999). Nonetheless, it is possible that IP_6 may regulate splicing
234 in some manner via interactions with both Prp8 and the NTC.

235 We were able to unambiguously assign three, connected long α-helices to Fyv6 (**Figure**
236 **4A**). These helices were visible in previous cryo-EM reconstructions of yeast C* and P complexes
237 but were either unassigned or misassigned. In the cases of misassigned densities, Fyv6 was
238 previously attributed to the C-terminal domain of the 1st step factor Yju2 (Wilkinson et al., 2017).
239 Yju2 also has an elongated helical architecture and adopts a similar position on C complex

240 (Wilkinson et al., 2021) and the post-P complex Intron Lariat Spliceosome (ILS) (Wan et al., 2017).
241 We closely inspected the density from previously determined spliceosome structures and
242 concluded that the Yju2 C-terminus is still a better fit than Fyv6 for densities in B*, C, and ILS
243 complexes, whereas Fyv6 is a better fit than Yju2 for densities in C* and P complexes (**figure 4-**
244 **figure supplement 1**). Therefore, this position of Fyv6 seems to be characteristic of a 2nd step
245 conformation of the spliceosome and consistent with the position of its distant human homolog
246 FAM192A in the human pre-C* complex (Zhan et al., 2022).

247 Fyv6 makes a multitude of interactions with essential splicing factors (**Figures 3B; 4E, F,**
248 **G**). One conserved region of Fyv6 is the N-terminus with a FVSE motif (**figure 4-figure**
249 **supplement 2**). This motif forms a 'hook' that interacts with a hydrophobic patch on the surface
250 of the Prp22 RecA2 domain, where it also forms hydrogen bonds by β-sheet augmentation
251 (**Figure 4E**). The hook is followed by three α-helices. The start of helix 2 sits on top of the intron
252 between the BP and the active site docked 3' SS, where it may act as a steric block to prevent 3'
253 SS undocking and promote exon ligation (**Figure 4F**) (S. Liu et al., 2017). Helix 2 also contains a
254 patch of conserved arginines that form salt bridges with Asp317 and Glu318 of Slu7 (**Figure 4F**).
255 The linker between helices 2 and 3 interacts with the NTC component Cef1, and helix 3 interacts
256 with NTC component Syf1 (**Figure 4G**). The binding interface with Syf1 overlaps with the
257 Syf1/Yju2 interaction in the C complex (Wilkinson et al., 2021), suggesting these interactions are
258 mutually exclusive (**Figure 4G**). Fyv6 thus provides a direct link between the Prp22 ATPase, NTC
259 components, and other essential splicing factors over a distance of ~100 Å.

260 By 3D classification, we were able to resolve a total of three states of the P-complex
261 spliceosome (**Figure 3C-E**). State I, represented by 51% of particles, is the most complete and
262 has all the above-described factors visible, including a stably-docked 3' SS. State II, represented
263 by 20% of particles, is similar to State I but lacks density for the N-terminal half of the 2nd step
264 factor Slu7. The endonuclease-like domain of Prp8, to which this domain of Slu7 binds, is

265 correspondingly shifted. Interestingly, this state retains strong density for the 3' SS, suggesting
266 the N-terminal regions of Slu7 are not involved in maintaining 3' SS docking after exon ligation.
267 Finally, State III, containing 29% of particles, entirely lacks density for the 2nd step factors Slu7,
268 Prp18, and Fyv6. Prp17 and the RNase H domain of Prp8 are still present but are weaker than in
269 States I and II, suggesting they are more flexible in State III. Most of Prp22 can still be observed
270 with weaker density except for the C-terminal domain that interacts with Prp8, which lacks density
271 entirely. Importantly, State III also lacks density for the 3' SS but has density for the 3' exon,
272 suggesting it is indeed post-catalytic and represents a state after loss of 2nd step factors and
273 undocking of the 3' SS from the catalytic core. The coincidence of loss of Fyv6 with loss of Prp18
274 and Slu7 reinforces the notion that these three factors act together and are important for 3' SS
275 docking, maintaining the 3' SS in the active site after exon ligation, and for stabilization of Prp17,
276 Prp22, and the RNase H domain of Prp8.

277 **The Fyv6/Syf1 Interaction is Critical for Suppressing *fyv6Δ* Phenotypes**

278 To determine the functionally critical regions and interactions of Fyv6, we used the cryo-
279 EM structure to design five truncation mutants (**Figure 5A**). The first three truncations remove
280 amino acids from the N-terminus of Fyv6: deletion of the first 16 amino acids, which are not
281 resolved in the cryo-EM structure (Δ1-16); deletion of the first 23 amino acids, which removes the
282 conserved hook region of Fyv6 that interacts with the Prp22 RecA2 domain (Δ1-23); and deletion
283 of amino acids 1 to 51, which additionally removes the first α-helix and interactions with Prp22,
284 Prp8, and Slu7 (Δ1-51). The remaining two mutants are C-terminal truncations. In the first, amino
285 acids 134 to 173, which do not have clear density in the cryo-EM structure and are not modeled
286 but which do contain a predicted nuclear localization signal (NLS), are deleted (Δ134-173)
287 (Nguyen Ba et al., 2009). In the second, amino acids 103 to 173 are deleted (Δ103-173), which
288 additionally removes the region of the protein that interacts with Syf1.

289 We tested each truncation mutant for its ability to suppress the *cs* and *ts* phenotypes of
290 the *fyv6Δ* strain when expressed from a plasmid under the native promoter (**Figure 5B**). All of the
291 N-terminal truncation mutations could suppress the *cs* or *ts* phenotypes to some degree.
292 Surprisingly, a strain with the complete deletion of the conserved hook domain that interacts with
293 Prp22 (Δ1-23) grew similarly to the strain expressing WT Fyv6. We wondered if splicing changes
294 could still be present even if the growth phenotype was suppressed; so, we assayed *SUS1*
295 isoforms by RT-PCR. We previously showed that loss of Fyv6 causes use of an alternative 3' SS
296 in the first intron of this pre-mRNA (Lipinski et al., 2023). In addition to suppression of the *fyv6Δ*
297 growth phenotype, the N-terminal truncation mutants also showed no evidence for changes in
298 *SUS1* splicing (**Figure 5C**). The N-terminal region of Fyv6 composed of the hook domain and the
299 first α-helix is not required for suppression of either the temperature sensitivity or splicing
300 phenotypes observed when Fyv6 is lost despite its conservation and interactions with critical
301 splicing factors (Prp8, Prp22, and Slu7).
302 For the C-terminal truncations, the Δ134-173 truncation was also able to suppress the *cs*
303 and *ts* phenotypes, indicating that the predicted NLS is also not essential (**Figure 5B**). However,
304 this mutant grew more poorly at 16°C than did the Δ1-16 and Δ1-23 truncations and showed some
305 evidence of alternative 3' SS usage in *SUS1* (**Figure 5C**). The largest effects were seen when the
306 C-terminus was truncated further. The Δ103-173 truncation strain phenocopied the *fyv6Δ* strain
307 and grew poorly at 37°C and was dead at 23° or 16°C (**Figure 5B**). Additionally, RT-PCR showed
308 increased use of the alternative 3' SS in *SUS1* with this truncation (**Figure 5C**). To determine if
309 this phenotype could be due to loss of protein expression, we assayed expression of the epitope-
310 tagged proteins by western blot (**figure 5-figure supplement 1A**). In all cases, we could detect
311 protein; however, the abundance of the N-terminally epitope-tagged Δ103-173 variant was much
312 lower than the others. Therefore, we also constructed a C-terminally epitope-tagged version of
313 Δ103-173 (**figure 5-figure supplement 1B**). The C-terminally-tagged protein expressed at much
314 higher levels but also failed to suppress the *cs* and *ts* phenotypes. These data suggest that the

315 C-terminal region of Fyv6 that includes a portion of α-helix 3 and the Syf1 interaction domain is
316 critical for function.

317 To obtain additional evidence for the importance of the Fyv6/Syf1 interaction, we created
318 a *syf1Δ* shuffle strain containing WT Fyv6 and expressed C-terminal Syf1 truncations (**Figure**
319 **5D**). We hypothesized that loss of the Fyv6-interacting domain on Syf1 would phenocopy *fyv6Δ*.
320 We observed just this effect. Loss of the Fyv6-interacting region in Syf1 Δ778-859 and Δ634-859
321 mutants resulted in either modest (Δ778-859) or severe (Δ634-859) *cs* and *ts* phenotypes. In
322 addition, these Syf1 truncation mutants also triggered use of the alternative 3' SS in *SUS1* (**Figure**
323 **5F**). Interestingly, if the Δ778-859 and Δ817-859 Syf1 mutants are expressed in a *fyv6Δ*
324 background, it results in suppression of the *fyv6Δ ts* phenotype (**Figure 5G; *c.f.* 5B**). However,
325 the *SUS1* alternative 3' SS is still used (**Figure 5H**). This indicates that *ts* phenotype suppression
326 and triggering usage of the alternative 3' SS in *SUS1* are separable processes.

327 When considered together, these results likely originate from mutually exclusive Fyv6/Syf1
328 and Yju2/Syf1 interactions. It is possible that in the absence of Fyv6, Syf1 inappropriately binds
329 Yju2 during exon ligation. The presence of Yju2 during the 2nd step could then lead to growth
330 defects that are suppressed when the Yju2-binding site on Syf1 is deleted. Alternatively or in
331 addition, the absence of Fyv6 could perturb the equilibrium between the 1st- and 2nd-step
332 conformations of the spliceosome and result in favoring of the 1st step (L. Liu et al., 2007). Loss
333 of this equilibrium could lead to growth defects that are suppressed by destabilization of the 1st-
334 step conformation by removing a binding site for Yju2 on Syf1 and restoring the equilibrium. In
335 both cases, truncation of Syf1 suppresses growth defects but not *SUS1* splicing defects since
336 Fyv6 function is still needed during the 2nd step.

337 **Mutations in Many Different Splicing Factors Can Suppress *fyv6Δ* Phenotypes**

338 To gain additional insights into Fyv6 function, we carried out a genetic screen to detect
339 spontaneously arising suppressors that can correct temperature-dependent growth defects
340 (**Figure 6A**). This method has previously been used to illuminate many aspects of spliceosome

341 biochemistry and non-silent mutations within splicing factors are likely causative for suppression
342 (Montemayor et al. 2014; Kuhn and Brow, 2000; Brow, 2019).

343 We plated saturated *fyv6Δ* yeast cultures onto 20 different YPD plates and incubated them
344 at 37°C until colonies arose. Within several days, colonies of various sizes appeared and were
345 isolated. A subset of picked colonies were then tested for suppression of the *ts* phenotype. All of
346 these colonies were able to suppress growth defects at 37°C, and many also suppressed the *cs*
347 phenotype at 23°C (**figure 6-figure supplement 1**). We then performed whole genome
348 sequencing on the largest of the picked colonies as these were expected to be the strongest
349 suppressors. In 19 of 20 sequenced strains, we were able to identify at least one non-silent
350 mutation in a splicing factor (**Figure 6B**, **supplementary table 5**). When we carried out a similar
351 experiment aimed at identifying *cs* suppressors, we were unable to identify any likely causative
352 mutations in splicing factors. Therefore, we focused our analysis on the *ts* suppressor mutations.

353 Collectively, the identified mutations tended to fall into two categories: gain of positive
354 charge or substitution with a bulkier side chain. Gain of positive charge mutations were found in
355 Prp8 (G1868R) as well as the second step factors Slu7 (A24R, and N28K), and Prp22 (I1133R).
356 Structurally, amino acids within Prp8 and Prp22 are proximal to RNA within the spliceosome and
357 addition of charged amino acid side chains may stabilize interactions with the phosphodiester
358 RNA backbone. The N-terminus of Slu7 containing A24 and N28 is not resolved in any
359 spliceosome structure to our knowledge and normally contains many negatively charged
360 residues. The majority of identified suppressors involve a mutation to a bulkier side chain including
361 several in Prp8 (S1594F/Y, V1862L), Prp17 (A251V, G386W), Cef1 (A37V), and Clf1 (T33I). The
362 increase in hydrophobic surface area provided by these mutations may help to stabilize
363 interactions with nearby proteins, compensating for structural destabilization due to the absence
364 of Fyv6. Alternatively, since Prp8, Prp17, Cef1, and Clf1 are all present during 5'SS cleavage, it
365 is possible that these bulky mutations could destabilize a 1st step conformation of the spliceosome

366 and suppress phenotypes due to the loss of Fyv6 by facilitating formation of the 2nd step
367 conformation.

368 We isolated one suppressor mutation within the U2 snRNA (A25G) near where the C-
369 terminal domain of Prp22 inserts towards the active site and located beneath the Fyv6 binding
370 site. It has previously been observed that mutation of this specific U2 snRNA nucleotide is not
371 deleterious to growth (McPheeters and Abelson, 1992) and is therefore well-tolerated by yeast.
372 The mechanism of suppression by this mutation is not clear; however, it is interesting to note that
373 we also observed suppressor mutations in the U2 snRNP component Rse1 (**supplementary**
374 **table 5**) which is released from the spliceosome prior to catalysis. The Rse1 mutations always
375 occurred coincident with mutations in other splicing factors. It is possible that suppressors in
376 factors present prior to or after exon ligation are able to suppress (or enhance suppression of)
377 *fyv6Δ* by changing how pre-mRNAs compete for a limited set of splicing factors or by reducing
378 blocks to pre-spliceosome assembly caused by accumulation of stalled complexes (Mendoza-
379 Ochoa et al., 2019; Munding et al., 2013). Together these data indicate that mutations in many
380 different splicing factors including second-step factors and the U2 snRNA can be isolated from
381 *fyv6Δ* suppressor strains.

382 **Multiple Second-step Splicing Defects can be Rescued by the Same Suppressor**

383 We decided to study several of these mutations in greater detail and to confirm that they
384 were sufficient for *fyv6Δ ts* phenotype suppression. In the case of Cef1, we obtained several
385 mutants located near the interface between Cef1 and the 2nd step factor Prp17: A37V, M175I, and
386 Q193P (**Figure 6C**). This interface has only been observed in structures of C* and P-complex
387 spliceosomes, suggesting its importance for exon ligation. In addition, it has previously been
388 reported that another mutant of Cef1 A37—A37P—is able to suppress splicing defects due to a
389 BS adenine to guanosine substitution (BS-G) which causes stalling after 5' SS cleavage (Query
390 and Konarska, 2012). Therefore, we wondered if other Cef1 mutants capable of suppressing
391 defects due to BS-G could also suppress *fyv6Δ* (Cef1 A37P, V36R, and S48R). We created *fyv6Δ*

392 shuffle strains for Cef1 and tested each mutant's ability to suppress *cs* and *ts* phenotypes (**Fig.**
393 **6D**). All of these Cef1 mutants, both those isolated from our suppressor screen and those
394 identified as BS-G suppressors, could at least weakly suppress the *cs* phenotype at 23°C with
395 our isolated M175I mutant being a particularly strong suppressor. In addition, all of the mutants
396 except Cef1 A37V could suppress the *ts* phenotype at 37°C to varying degrees. These results
397 confirm that single point mutants in Cef1 can suppress *fyv6Δ* growth phenotypes and that at least
398 some BS-G suppressors in Cef1 also suppress *fyv6Δ*. A common mechanism could be that these
399 mutations stabilize the exon ligation conformation of the spliceosome to favor the 2nd step either
400 when a BS-G is present or Fyv6 is absent.

401 In the case of Prp8, we tested five different suppressor mutations in *prp8* shuffle strains
402 (**Figure 6E, F**). Two of these are located within the Prp8 α-finger domain (S1584F,Y; **Figure 6E**)
403 while the remainder are located within the RNase H-like domain β-finger (V1862L, G1868R,
404 T1982S; **Figure 6C, 6E**). We confirmed that four of the identified Prp8 suppressor mutations could
405 partially suppress either or both of the *cs* and *ts fyv6Δ* phenotypes (**Figure 6F**; S1574Y, V1862L,
406 G1868R, and T1982S). Even though we isolated the Prp8 S1584F mutant in our screen and this
407 substitution is very similar to S1584Y, we were not able observe suppression due to this mutant
408 in these strains. Identification of mutants in Prp8 that suppress *fyv6Δ* is not surprising since many
409 different alleles of Prp8 are known to modulate the conformational equilibrium between the 1st
410 and 2nd steps (Fica and Nagai, 2017; L. Liu et al., 2007; Query and Konarska, 2004) or other steps
411 in splicing. Indeed, suppressors in Prp8 have previously been identified at some of these same
412 positions: V1862A/Y/D and T1982A were identified as suppressors of, respectively, the *U4-cs*1
413 allele (Kuhn and Brow, 2000; Kuhn et al., 1999) or the 5' SS U2A mutant (Siatecka et al., 1999).

414 Finally, given our observations with the Cef1 and Prp8 mutants, we wondered about the
415 generality of 2nd step splicing factor suppression. Several dominant mutants in the 2nd step factor
416 Prp18 were previously shown to suppress *ts* phenotypes due to various mutations in Slu7
417 (Aronova et al., 2007). We wondered if these Prp18 mutants would also suppress the *ts* (or *cs*)

418 phenotype due to Fyv6 loss. Indeed, the Prp18 V191A suppressor of *slu7* alleles was able to
419 improve growth at 37°C of *fyv6Δ* yeast (**figure 6-figure supplement 2**). Together our results from
420 the suppressor analysis support a model in which a given 2nd step suppressor mutation may be
421 able to restore splicing activity lost by a variety of mechanisms.

422 **A Prp22-Dependent Splicing Stall is Relieved by Fyv6 Deletion**

423 The final *fyv6Δ* suppressor mutation that we studied was the Prp22 I1133R mutant. This
424 mutation is located within the C-terminal domain of Prp22 that enters the spliceosome active site
425 and is located proximal to U2 snRNA nucleotide A31 (**Figure 7A**). Fyv6 bridges over this Prp22-
426 U2 snRNA interaction. The I1133R mutation might stabilize Prp22/U2 snRNA contacts that can
427 compensate for Fyv6 loss and promote exon ligation. The Prp22 I1133R mutant is able to weakly
428 suppress both the *cs* and *ts* phenotypes in *fyv6Δ* yeast (**Figure 7B, C**). Given its location in the
429 C-terminal domain, we wondered if it or *fyv6Δ* would show synthetic genetic interactions or
430 epistasis with mutations in the helicase domain. We tested two helicase domain mutations, R805A
431 and G810A, both of which are known to impact Prp22-dependent proofreading (Mayas et al.,
432 2006). The Prp22 R805A mutant is by itself *cs* (Schwer and Meszaros, 2000) and showed a
433 synthetic lethal interaction with *fyv6Δ* (**Figure 7B, 7C**). This was only slightly rescued by
434 simultaneously introducing I1133R into Prp22. In contrast, Prp22 G810A mutant is viable in the
435 presence and absence of Fyv6 as well as in combination with the I1133R suppressor mutation
436 (**Figure 7B, 7C**). Prp22 G810A by itself does not suppress the *ts fyv6Δ* phenotype; however, the
437 Prp22 G810A/I1133R double mutant is a stronger suppressor of the *ts* phenotype than either
438 mutant alone. These additive genetic interactions suggest that the Prp22 *fyv6Δ* suppressor
439 mutation (I1133R) and the helicase domain mutations (R805A and G810A) impact distinct Prp22
440 functions. These functions could correspond to Prp22's role in promoting exon ligation during the
441 2nd step (the C-terminal domain mutation) and its role in promoting ATP-dependent mRNA release
442 and proofreading (the helicase domain mutations).

443 Recently, it was reported that the Prp22 G810A mutant could activate usage of some
444 alternative 3' SS that are also activated by *PRP18* deletion (Roy et al., 2023). We therefore
445 wondered if any of the Prp22 mutants could activate alternative 3' SS also activated by *FYV6*
446 deletion. We isolated RNA from these strains and analyzed *SUS1* splicing by RT-PCR (**Figure**
447 **7D, E**). None of the Prp22 mutants activated usage of the *SUS1* alternative 3' SS or enhanced
448 usage of this site beyond what is observed upon Fyv6 deletion. However, we noticed that the
449 Prp22 helicase mutants, R805A and G810A, both caused an accumulation of unspliced pre-
450 mRNA. This is consistent with these mutations causing a block during pre-mRNA splicing and
451 having a different effect on splicing than Prp22 I1133R. Surprisingly, the block due to the G810A
452 mutation was relieved in the *fyv6Δ* strains and little pre-mRNA accumulation was observed in the
453 absence of Fyv6. This result suggests that Fyv6 could act as a negative regulator of splicing of
454 the *SUS1* transcript when a Prp22 helicase domain mutant is present. Removing Fyv6 restores
455 splicing by activation of the *SUS1* BP proximal 3' SS.

456 To further explore the connections between Fyv6 and Prp22 fidelity, we used the ACT1-
457 CUP1 assay in which yeast growth in the presence of increasing concentrations of Cu^{2+} is
458 proportional to the extent of splicing of a reporter RNA (**Figure 7F, G**; **figure 7-figure supplement**
459 **1, 2**). Since the Prp22 R805A mutant grew poorly, we only assayed the Prp22 G810A, I1133R,
460 and G810A/I1133R (double) mutants in the presence and absence of Fyv6. Consistent with
461 previous results, we found that *fyv6Δ* is deleterious for splicing of the WT ACT1-CUP1 reporter
462 containing consensus splice sites. Copper tolerance was improved when *fyv6Δ* was combined
463 with Prp22 I1133R. Unexpectedly, Prp22 I1133R was deleterious when Fyv6 was present for this
464 reporter. If this Prp22 mutant and Fyv6 both promote the 2nd step, then their combination may
465 have an additive, negative effect on splicing due to over-stabilization of this spliceosome
466 conformation.

467 Finally, we assayed strains containing a 3' SS UAG to gAG reporter since it was previously
468 shown that Prp22 helicase domain mutants could increase usage of nonconsensus 3' SS due to
469 faulty proofreading activity (**Figure 7F, G**). In agreement with this, we observed a dramatic
470 increase in copper tolerance when Prp22 contained both the C-terminal domain and helicase
471 mutants (double). This suggests that splicing of nonconsensus 3' SS splice sites is enhanced both
472 by stabilization of the 2nd step conformation (I1133R) and perturbing mRNA release (G810A). This
473 effect on Prp22 is Fyv6-dependent since loss of Fyv6 results in very poor copper tolerance of
474 strains containing the gAG reporter, likely since this 3' SS is located far from the BP (38 nt). These
475 results show that *fyv6Δ* can be suppressed with a Prp22 C-terminal domain mutant and that
476 mutations in the Prp22 C-terminal domain can have distinct functional consequences from those
477 located in the helicase domain. In the case of *SUS1*, stalling of splicing due to the Prp22 G810A
478 mutant can be relieved by removing Fyv6 and activation of a BP proximal 3' SS.

479 **DISCUSSION**

480 Here, we establish Fyv6 as a 2nd step splicing factor in yeast that promotes usage of BP-
481 distal 3' SS. Structural, genetic, and biochemical studies reveal critical contacts and interactions
482 between Fyv6 and the splicing machinery. From these data, we propose that Yju2/Syf1
483 interactions need to be disrupted for proper Fyv6 recruitment and that Fyv6 can enforce the
484 Prp22-dependence of at least some splicing events. Combined, our data allow us to propose a
485 model for Fyv6's role during the 2nd step (**Figure 8**). In this model, Fyv6 is recruited to the C*
486 complex after Prp16-dependent release of Yju2, which exposes the binding site for Fyv6 on Syf1.
487 Once bound, Fyv6 (possibly in concert with Slu7 and Prp18) facilitates docking of BP distal 3' SS
488 into the active site. In the absence of Fyv6, the use of BP distal 3' SS becomes more difficult and
489 BP proximal 3' SS are favored. Under these conditions, the requirement for Prp22 during exon
490 ligation is reduced and Yju2 may also potentially rebind Syf1. One or both of these factors could
491 contribute to formation of a lower fidelity spliceosome with relaxed sequence constraints for exon
492 ligation.

493 **Structural Insights into the Recruitment and Release of 2nd step Factors**

494 A key principle of spliceosome structural biochemistry is the presence of mutually
495 exclusive interactions that coordinate the stepwise and directional progression of splicing
496 (Townsend et al., 2020). Our cryo-EM structure of the P complex spliceosome suggests another
497 such interaction is involved in the 1st to 2nd-step transition during which Fyv6 displaces Yju2. Yju2
498 and Fyv6 occupy overlapping binding sites on the splicing factor Syf1 and, in fact, unassigned
499 density in spliceosome P complexes due to Fyv6 was previously mis-interpreted as Yju2 due to
500 their structural similarity (Wilkinson et al., 2017; Wilkinson et al., 2021). We propose that Prp16-
501 promoted spliceosome remodeling results in release of Yju2 from the spliceosome C complex and
502 permits mutually exclusive binding of Fyv6. Fyv6 remains bound in the P complex but then may
503 dissociate to permit re-binding of Yju2, which was observed by cryo-EM to be a component of the
504 yeast ILS complex (Wan et al., 2017). It should be noted, however, that intron-lariats only weakly
505 co-immunoprecipitate with Yju2 (Y.-C. Liu et al., 2007) and that Yju2's presence in the cryo-EM
506 data for ILS complexes could originate from the complexes being purified with a TAP-tag on Yju2
507 itself (Wan et al., 2017). Since Yju2 has also not been observed in metazoan ILS complexes, its
508 role in spliceosome disassembly and the need for Fyv6-Yju2 exchange during the P to ILS
509 transition should be studied further.

510 Previously, Chiang and Cheng noted that while the N-terminal half of Yju2 was able to
511 restore 1st step activity to Yju2-depleted extracts, it is much more stably associated if a second
512 polypeptide containing the C-terminal, Syf1-interacting half was included (Chiang and Cheng,
513 2013). It is possible that competition between Yju2 and Fyv6 for Syf1 binding can explain these
514 results. If only the N-terminal half of Yju2 is present, Fyv6 could associate prematurely with Syf1
515 and result in destabilization of the 1st step conformation in favor of 2nd step interactions. This may
516 then result in weaker binding for the N-terminal half of Yju2. Failure to properly recruit and
517 exchange the Yju2/Fyv6 interaction on Syf1 may also be the origin of some of the yeast growth
518 and splicing phenotypes we observe (**Figure 5**).

519 The need for Yju2/Fyv6 exchange hints at two distinct functions for Fyv6: a role in Yju2
520 displacement to prevent its re-binding during exon ligation and a role in stabilization of the 2nd
521 step spliceosome conformation. These two functions can potentially result in the distinct *cs* and
522 *ts* phenotypes in yeast. While more work is needed to dissect these phenotypes, it is possible that
523 the *cs* phenotype results from increased stability of the Yju2/Syf1 interaction at lower
524 temperatures and the need for Fyv6 to act as a competitor of this interaction. The *ts* phenotype
525 on the other hand may result from destabilization of the 2nd step conformation of the spliceosome
526 active site due to loss of Fyv6. It is possible that loss of Fyv6 results in destabilization due to
527 removal of a buttress that holds the RNase H-like domain of Prp8 in place (along with Prp18),
528 changes in how the C-terminal domain of Prp22 interacts with the spliceosome active site,
529 removal of an impediment to reversal of the U2 snRNA/BS duplex conformational change that
530 occurs during the C to C* complex transition, or a combination of these factors.

531 The high quality of our cryo-EM data combined with 3D classification also provide new
532 insights into the requirements for 3' SS docking into the active site and potentially for how the P
533 complex spliceosome is disassembled into the ILS complex. It was previously speculated that the
534 N-terminal domain of Slu7 may be critical for 3' SS docking by reducing the entropic cost of this
535 process when the BP to 3' SS distance is long (Wilkinson et al., 2017). In our state II P complex
536 structure, the 3' SS remains docked but this domain of Slu7 is not observed. This suggests that
537 either Slu7 N-terminal domain interactions with Cwc22 and Prp8 are not essential for 3' SS
538 docking into the active site for exon ligation and/or that these interactions are not essential for
539 maintaining 3' SS docking within P complex once they form in C*.

540 In the state III P complex structure, densities for the 2nd step factors Fyv6, Prp18, and Slu7
541 are entirely missing and the 3' SS is no longer docked into the active site. While it is possible that
542 this may reflect decomposition of the P complex (or another intermediate) by a pathway unrelated
543 to cellular spliceosome disassembly, the structure is suggestive that 3' SS undocking is coupled
544 to 2nd step factor release. These steps may be necessary to help prepare the spliceosome for ILS

545 complex formation since the 3' SS is undocked in all ILS structures obtained to date (Vorländer
546 et al., 2024; Wan et al., 2017; Yan et al., 2015; Zhang et al., 2019). Prp22 is still present in this
547 structure, and it is possible that state III represents a conformation occurring after exon ligation
548 but prior to Prp22-dependent mRNA release. In this case, the state III structure implies that Prp22
549 ATPase activity is not needed for dissociation of Fyv6, Prp18, and Slu7. It is also interesting to
550 note that the C-terminal domain of Prp22 can no longer be resolved in the state III structure. What
551 exactly activates the Prp22 ATPase to promote proofreading or mRNA release is not known. It is
552 conceivable that undocking of the 3' SS from the active site can be sensed by the Prp22 C-
553 terminal domain and this contributes to ATPase activation. This model differs from that previously
554 proposed for Prp22-enabled 3' SS sampling in which that ATPase activity of Prp22 is needed to
555 undock the 3' SS (Semlow et al., 2016). However, sampling could involve multiple steps: ATP-
556 independent 3' SS undocking and ATP-dependent entry into the sampling state. Whether or not
557 the 2nd step factors must release or alter conformation to enable sampling is unknown. Regardless
558 of the exact mechanism, it is important to recognize that the P complex structures determined
559 here were all obtained using a Prp22 mutant defective in mRNA release. The chemical and kinetic
560 competencies of these states will require future investigations.

561 **Multiple, Non-Redundant 2nd Step Factors Promote Use of BP Distal 3' SS**

562 The challenge of 3' SS selection involves not just selection of the correct nucleotide
563 sequence (YAG) but also identifying which YAG sequence to use. Here, we define a function for
564 Fyv6 in facilitating use of BP distal 3' SS, especially those located $\geq$ 21 nt away from the branch.
565 This function is similar to those of other 2nd step factors important for efficient splicing when the
566 BP-3' SS distance is $\geq$12 nt (Slu7, Prp18) or $\geq$21 nt (Prp22) (Brys and Schwer, 1996; Schwer and
567 Gross, 1998; Zhang and Schwer, 1997). Human Slu7 has additionally been reported to be
568 important for preventing suppression of the correct 3' SS in favor of up- or downstream alternative
569 3' SS (Chua and Reed, 1999). Our previous study using competing 3' SS in the ACT1-CUP1
570 intron did not provide evidence for suppression of the correct 3' SS in the absence of Fyv6,

571 suggesting that this function is not shared between human Slu7 and yeast Fyv6. Nonetheless, it
572 is important to recognize that the splicing machinery employs multiple factors that enforce usage
573 of BP distal 3' SS. These functions are not redundant as changes in 3' SS are still observed in the
574 absence of Fyv6 but presence of Prp18 and vice versa (Roy et al., 2023).

575 Intron architecture can also contribute to 3' SS selection since canonical “AG” 3' SS are
576 depleted in humans in the region between the BP and annotated 3' SS (the AG exclusion zone,
577 or AGEZ) (Corvelo et al., 2010; Gooding et al., 2006). AG sites are also typically depleted in the
578 corresponding region in yeast introns (data not shown). This would suggest that annotated 3' SS
579 are also the most optimal sites located downstream of the BP. However, an important assumption
580 of this model is that non-AG 3' SS can also be effectively proofread and not used. Deletion of
581 either Prp18 or Fyv6 leads to activation of not just BP proximal 3' SS but also those with highly
582 divergent sequences from the YAG consensus (Roy et al., 2023). This suggests that an AGEZ
583 alone is insufficient for correct 3' SS usage and that mechanisms to ensure preferential use of
584 YAG sites are critical.

585 It is likely that Fyv6 and Prp18 enforce usage of YAG sites by common as well as factor-
586 specific mechanisms. Both proteins stabilize the conformation of the Prp8 RNase H-like domain
587 in P complex. Numerous splice site suppressor mutations map to this domain including those that
588 enhance splicing of non-YAG 3' SS (Galej et al., 2013). Fyv6 and Prp18 may be essential for
589 establishing a “high fidelity” conformation of the RNase H-like domain that enforces use of
590 canonical YAG 3' SS and preventing activation of cryptic sites within the AGEZ. In support of this,
591 we note that in our state III P complex structure that lacks both Fyv6 and Prp18 and a stably
592 docked 3' SS, the RNase H-like domain is also more flexible.

593 In addition to this possibility, Fyv6 and Prp18 may also contribute uniquely to 3' SS fidelity
594 and selection. The conserved loop region of Prp18 inserts into the spliceosome active site and
595 contacts the 3' SS. Partial deletion of this region of Prp18 phenocopies at least some of the
596 changes in 3' SS selection when Prp18 is deleted entirely (Crotti et al., 2007; Roy et al., 2023).

597 This indicates that even when the Prp8 RNaseH-like domain is still stabilized by Prp18 (and Fyv6)
598 disruptions to 3' SS selection can still occur. Unlike Prp18, Fyv6 does not contact the spliceosome
599 active site. However, it is the only 2nd step factor that contacts exon ligation fidelity factor Prp22.
600 While these contacts are not essential for suppressing use of an alternative 3' in *SUS1*, a mutation
601 in Prp22 can nonetheless suppress a *fyv6Δ* phenotype and loss of Fyv6 relieves a Prp22 helicase
602 mutant-dependent stall in *SUS1* splicing. These observations suggest that Fyv6 and Prp22 are
603 functionally connected to one another.

604 **Some 2nd Step Factors May Enforce Usage of Prp22 during Exon Ligation**

605 We were particularly struck by the similarities in the BP-3' SS distances for the requirement
606 of Prp22 during exon ligation and for promotion of BP distal 3' SS usage by Fyv6, both $\geq$21 nt
607 (Schwer and Gross, 1998). In addition, the alternative, BP proximal 3' SS that are activated when
608 Fyv6 is deleted show much less sequence conservation relative to the annotated 3' SS and
609 include sequences (GAG, BG) known to be proofread and rejected by Prp22. Together, this
610 suggests that one function of Fyv6 is to enforce Prp22-dependence of exon ligation by stabilizing
611 a spliceosome conformation that more easily enables usage of BP distal 3' SS (**Figure 8**). As
612 these sites require Prp22 for exon ligation, it is also likely that they are subject to Prp22-dependent
613 proofreading, and this may enforce accurate exon ligation at the YAG 3' SS consensus. When
614 Fyv6 is absent, many alternative, BP proximal 3' SS are activated. These sites could have a
615 relaxed requirement for Prp22 and proofreading. While the Fyv6-dependence of Prp22 occupancy
616 is beyond the scope of the current manuscript, loss of Prp18 (which also activates usage of non-
617 canonical, BP-proximal 3' SS) does result in lower occupancy of Prp22 on the *ACT1* intron
618 (Strittmatter et al., 2021). This suggests that Prp22 occupancy, and possible involvement in the
619 exon ligation step, can be influenced by 2nd step factors.

620 There is precedent for nonessential splicing factors enforcing use of a proofreading
621 ATPase. Cus2 is not essential for pre-spliceosome formation (Yan et al., 1998). However, when
622 Cus2 is present then ATPase activity of Prp5 is essential for disruption of the Hsh155/Cus2

interaction (Perriman et al., 2003; Talkish et al., 2019). In this case, Cus2 is not essential for Prp5 proofreading of BP selection, and the connection between the ATP hydrolysis activity of Prp5, removal of Cus2, and proofreading is unclear (Liang and Cheng, 2015; Talkish et al., 2019; Xu and Query, 2007). It is possible that enforcement of Prp5 ATPase activity by Cus2 is important for other aspects of pre-spliceosome formation *in vivo* and the impact of Prp5 and Cus2 on BP selection has not yet been studied transcriptome-wide using high-resolution, sequencing-based approaches. The C-terminal domain of the 1st step splicing factor Yju2 (the same domain that competes with Fyv6 for Syf1 binding) is also not essential for 5' SS cleavage. In the absence of this domain, the N-terminal domain of Yju2 is sufficient for promoting the 1st step reaction, and the spliceosome can transition to the 2nd step and carry out exon ligation without Prp16, albeit inefficiently (Chiang and Cheng, 2013). Importantly, addition of the C-terminal domain on a separate polypeptide reduces Prp16-independent activity. This suggests that the Yju2 C-terminal domain enforces the use of the Prp16 ATPase. As we propose with Fyv6 and Prp22, the C-terminal domain of Yju2 may not just help to promote the 1st to 2nd step transition by enforcing Prp16-dependence but could also facilitate Prp16-dependent proofreading during 5' SS cleavage (Koodathingal et al., 2010; Semlow et al., 2016). General operating principles of the yeast splicing machinery may not just include proofreading but also use of splicing factors that enforce usage of the proofreading ATPases.

MATERIALS AND METHODS

Key Resources Table				
Reagent type (species) or resource	**Designation**	**Source or reference**	**Identifiers**	**Additional information**

strain, strain background (*Saccharomyces cerevisiae*)	Various S. cerevisiae strains			See Supplementary Table 6 for full list
recombinant DNA reagent	Various plasmids			See Supplementary Table 7 for full list
Sequence-based reagent	Various oligonucleotides			See Supplementary Table 8 for full list
antibody	Anti-FLAG (Mouse monoclonal)	Sigma-Aldrich	Cat #: F1804; RRID:AB_262044	WB (1:1000)
antibody	Anti-actin (mouse monoclonal)	Sigma-Aldrich	Cat #: MAB1501; RRID:AB_2223041	WB (1:5000)
antibody	Anti-mouse IgG – HRP (Goat polyclonal)	Bio Rad	Cat #: 1706516; RRID:AB_11125547	WB (1:8000)
peptide, recombinant protein	Bovine Serum Albumin	Sigma	Cat#: A7906	

commercial assay or kit	Clarity Western ECL substrate	Bio Rad	Cat #: 1705060	
commercial assay or kit	Monarch RNA Cleanup Kit (50 ug)	New England Biolabs	Cat #: T2040	
commercial assay or kit	TURBO DNA-free kit	Thermo Fisher Scientific	Cat #: AM1907	
commercial assay or kit	TruSeq Stranded mRNA kit	Illumina	Cat #: 20020594	
commercial assay or kit	Master Pure Yeast RNA Purification kit	LGC Biosearch Technologies	Cat #: MPY03100	
commercial assay or kit	Access RT-PCR System	Promega	Cat #: A1250	
chemical compound, drug	Ni-NTA agarose	Qiagen	Cat #: 30210	
chemical compound, drug	Amylose resin	New England Biolabs	Cat #: E8022S	
chemical compo	Fluorescein-5-thiosem	Sigma-Aldrich	Cat #: 46985-100MG-F	

und, drug	icarbazide			
software, algorithm	RELION-5.0	Kimanius et al., 2024; doi: 10.1038/s41592-024-02304-8	RRID:SCR_016274	https://relion.readthedocs.io/en/latest/index.html
software, algorithm	Topaz	Bepler et al., 2019; doi: 10.1038/s41592-019-0575-8		https://cb.csail.mit.edu/topaz/
software, algorithm	Coot	Casañal et al., 2020; doi: 10.1002/pro.3791	RRID:SCR_014222	https://www2.mrc-lmb.cam.ac.uk/personal/pemsley/coot/
software, algorithm	ISOLDE	Croll, 2018; doi: 10.1107/S2059798318002425	RRID:SCR_025577	https://tristanic.github.io/isolde/
software, algorithm	PHENIX	Liebschner et al., 2019; doi: 10.1107/S2059798319011471	RRID:SCR_014224	https://phenix-online.org/
software, algorithm	UCSF ChimeraX	Petterson et al., 2021; doi: 10.1002/pro.3943	RRID:SCR_015872	http://www.cgl.ucsf.edu/chimerax/
software, algorithm	R Project for Statistical Computing	R Foundation for Statistical Computing	RRID:SCR_001905	https://www.r-project.org/
software, algorithm	FASTQC	Andrews, 2010	RRID:SCR_014583	http://www.bioinformatics.babraham.ac.uk/projects/fastqc/
software,	Fastp	Chen et al., 2018; doi:10.1093/bioi	RRID:SCR_016962	https://github.com/OpenGene/fastp

algorithm		nformatics/bty560		
software, algorithm	STAR	Dobin et al., 2013; doi: 10.1093/bioinformatics/bts635	RRID:SCR_004463	https://github.com/alexdobin/STAR/releases
software, algorithm	SAMtools	Li et al., 2009; doi: 10.1093/bioinformatics/btp352	RRID:SCR_002105	https://www.htslib.org/
software, algorithm	Salmon	Patro et al., 2017; doi: 10.1038/nmeth.4197	RRID:SCR_017036	https://combine-lab.github.io/salmon/
software, algorithm	DeSeq2	Love et al., 2014; doi: 10.1186/s13059-014-0550-8	RRID:SCR_015687	https://bioconductor.org/packages/release/bioc/html/DESeq2.html
software, algorithm	feature Counts	Liao et al., 2014; doi: 10.1093/bioinformatics/btt656	RRID:SCR_012919	https://bioconductor.org/packages/release/bioc/html/Rsubread.html
software, algorithm	Splice Wiz	Wong et al., 2024; doi: https://doi.org/10.1093/bib/bbad468		https://github.com/alexchwong/SpliceWiz
software, algorithm	Image J 1.53v	Schneider et al., 2012; doi:10.1038/nmeth.2089	RRID:SCR_003070	https://imagej.net/ij/
other	Cryo-EM grid	Quantifoil	Cat #: Q350CR2-2NM	
other	NuPAGE Bis-Tris mini protein gel	Invitrogen	Cat #: NP0322	

other	NuPAGE™ MES SDS Running Buffer	Invitrogen	Cat #: NP0002	
other	Standard Vitrobot Filter Paper, Ø55/20 mm, Grade 595	Ted Pella	Cat #: 47000-100	
other	Mixed cellulose ester filter paper	Whatman	WHA7140104	
other	TRIzol	Thermo Fisher Scientific	Cat #: 15596018	
other	SuperScript III reverse transcriptase	Thermo Fisher Scientific	Cat #: 18080044	
other	Zymolyase	Zymo Research	Cat #: E1005	Used at 50 U/mL

643

644 **Yeast growth and culture**

645 Yeast transformation, plasmid shuffling/5-FOA selection, and growth were carried out
646 using standard techniques and media (Treco and Lundblad 1993; Sikorski and Boeke 1991).

647 **Cryo-electron microscopy**

648 <u>Purification of dominant-negative Prp22</u>

649 Yeast Prp22 with a dominant-negative S635A mutation was cloned into pRS424 and
650 pRS426 vectors after an N-terminal CBP-His-TEV tag (Galej et al., 2013). The protein was
651 expressed in 24 L of BCY123 yeast cells essentially as described (Galej et al., 2013).
652 Recombinant Prp22 was then purified first by Calmodulin-Sepharose in a buffer containing 50
653 mM Tris-HCl pH 8.5, 350 mM NaCl, 2 mM $CaCl_2$, 1 mM Mg acetate, 1 mM imidazole, 0.1% NP-
654 40 substitute, 5 mM β-mercaptoethanol and eluted with 3 mM EGTA. The protein was dialyzed
655 into 20 mM Tris-HCl pH 7.4, 350 mM NaCl, 10 mM imidazole, 0.1% NP-40 substitute and further
656 purified over Ni-NTA resin at 500 mM NaCl and eluted with 200 mM imidazole. The eluted protein
657 was treated with His-tagged TEV protease during dialysis against 20 mM HEPES-KOH pH 7.9,
658 300 mM KCl, 0.2 mM EDTA, 20% glycerol, 0.5 mM DTT, before removal of the protease with Ni-
659 NTA resin. The final protein was frozen in liquid nitrogen and stored at -80 °C.

660 Preparation and purification of P complex for cryo-EM

661 P complex was purified as described in (Wilkinson et al., 2017). Brr2-TAPS yeast were
662 grown in a 120 L fermenter and splicing extract was prepared by the liquid nitrogen method
663 essentially as previously described (Lin et al., 1985). A pre-mRNA substrate consisting of 20 nt
664 5'-exon, 95 nt intron, and 32 nt 3'-exon from the UBC4 pre-mRNA followed by 3xMS2 stem loops
665 was generated by run-off in vitro transcription from an EcoRI-linearized plasmid template. The
666 RNA product was labelled at the 3' end with fluorescein-5-thiosemicarbazide (Wu et al., 1996). A
667 180 mL in vitro splicing reaction was performed containing 60 mM potassium phosphate pH 7, 2
668 mM ATP, 2.5 mM $MgCl_2$, 3% w/v PEG8000, 3 nM pre-mRNA, 37.5 nM MS2-MBP protein, and
669 40% (v/v) splicing extract treated with dominant negative Prp22 S635A. Reactions were incubated
670 for 30 min at 23°C, then incubated for 20 min with 5 mM of a DNA oligonucleotide complementary
671 to the 3'-exon (oligo sequence 5'-ATGAAGTAGGTGGAT-3') to induce cleavage of the 3'-MS2 tag
672 by the endogenous RNase H activity of the splicing extract. The reaction mixture was centrifuged
673 through a 40% glycerol cushion in buffer A (20 mM HEPES, pH 7.9, 75 mM KCl, 0.25 mM EDTA).

674 The cushion was collected and applied to amylose resin in the presence of 0.025% NP-40
675 substitute. After overnight incubation at 4ºC the resin was washed and eluted with buffer A
676 containing 5% glycerol, 0.01% NP-40 substitute and 12 mM maltose. Fractions containing
677 spliceosomes were concentrated to 0.1 mg/mL then dialyzed against buffer A for 3 h.

678 For cryo-EM grid preparation, a freshly glow-discharged Cu300 R2/2 holey carbon grid
679 with a 2-nm layer of amorphous carbon (Quantifoil) was mounted in the chamber of a Vitrobot
680 Mark IV (Thermo Fisher Scientific) maintained at 4°C and 100% humidity. Spliceosomes (3 µL)
681 were applied and after 60 s was manually blotted using Ø55 grade 595 filter paper (Ted Pella),
682 followed by application of another 3 µL of spliceosomes, waiting 60 s, before blotting again and
683 plunging into liquid ethane.

684 Cryo-EM data collection

685 Cryo-EM data were collected as two datasets from two grids made from the same sample.
686 Dataset 1 was acquired using a Thermo Scientific Titan Krios cryo-TEM (LMB Krios 1) and dataset
687 2 was acquired using a Thermo Scientific Titan Krios G3i cryo-TEM (LMB Krios 3). Both used a
688 K3 direct detector (Gatan) operated in super-resolution mode with 2-fold binning, and an energy
689 filter with slit width of 20 eV. Micrographs were collected automatically using EPU in AFIS mode,
690 yielding a total of 51,113 movies at 81,000x or 130,000x magnification with a real nominal pixel
691 size of 0.93 Å or 0.669 Å, with defocus ranging from -1.3 µm to -3.1 µm and a total fluence per
692 micrograph of 40 $e^-/Å^2$, fractionated into 40 frames.

693 Cryo-EM data processing

694 All cryo-EM data were processed using RELION-5.0 (Kimanius et al., 2024). Both datasets
695 were initially processed separately. Movies were corrected for motion using the RELION
696 implementation of MotionCor2, with 4x4 patches and dose-weighting. CTF parameters were
697 estimated using CTFFIND-4.1. Particle picking was done using Topaz with the general model
698 (Bepler et al., 2019), yielding 1,820,457 particles. 3D classification was performed on 4-fold

699 (dataset 1) or 5-fold (dataset 2) binned particles using a P-complex reference map (EMD-10140),
700 and 299,741 (dataset 1) or 599,123 (dataset 2) were selected and refined to 2.99 Å or 2.78 Å
701 resolution respectively. After Bayesian Polishing and CTF refinement (per-particle defocus,
702 anisotropic magnification, beam tilt, trefoil, and 4th order aberrations) the resolution improved to
703 2.67 Å or 2.32 Å respectively. To improve the general density quality, 3D classification without
704 alignment was performed with a soft mask around the whole complex with T=15. Particles with
705 good density, without selecting for Fyv6 occupancy, were selected (151,443 and 257,501 for
706 datasets 1 and 2) and refined to 2.66 Å or 2.27 Å respectively. The particles were then merged,
707 refined, and then refined for anisotropic magnification. The overall scaling factors from the
708 "anisotropic" magnification matrix was then used to calculate the corrected pixel size for dataset
709 1 as 0.94057 Å, keeping dataset 2 constant at 0.669 Å per pixel. Defocus values for dataset 1
710 were then scaled by the square of 0.94057 / 0.93, with an empirical constant correction of -10.06
711 Å (Wilkinson et al., 2019). Finally, another round of per-particle defocus refinement and
712 anisotropic magnification refinement was performed to reduce errors in defocus correction and
713 dataset scaling. The combined particles refined to 2.24 Å resolution. Resolution is reported using
714 the gold-standard Fourier Shell Correlation with 0.143 cutoff.

715 The refined particles after merging were subjected to 3D classification without alignment,
716 with a soft mask around the entire spliceosome, with T=15. The resulting four classes were used
717 to define States I, II and III. To improve the densities for the periphery of the spliceosome that
718 displayed local flexibility, focused refinements were used with Blush regularization in RELION-5
719 to reduce overfitting (Kimanius et al., 2024). The Prp22 density was improved using a soft-mask
720 just around the Prp22 helicase domain for refinement of particles from States I and II, yielding a
721 2.96 Å map. Densities for the U2 snRNP, NTC, U5 Sm ring, and Cwc22 N-terminal domain were
722 each improved first by 3D classification without alignment of particles from all three states,
723 selecting particles with strong density (72,869 for the U2 snRNP, 260,409 for the NTC, 113,561
724 for the U5 Sm ring, 201,984 for Cwc22-NTD), performing signal subtraction to remove density for

725 the rest of the spliceosome (recentering on the mask center of mass and re-boxing to 300 pixels,
726 or 192 pixels for Cwc22-NTD), and finally 3D refinement starting with 1.8 degree local angular
727 searches, giving 3.42 Å for the U2 snRNP, 3.72 Å for the NTC, 3.06 Å for the U5 Sm, and 3.57 Å
728 for Cwc22-NTD. In all cases, control refinements without Blush regularization did not produce
729 interpretable maps (**figure 3-figure supplement 4).**

730 Model building

731 The model was built using Coot (Casañal et al., 2020) and ISOLDE (Croll, 2018) starting
732 with PDB 6EXN (Wilkinson et al., 2017) as an initial model for the core and PDB 7B9V (Wilkinson
733 et al., 2021) as an initial model for the periphery. The core was improved by manual fixing in Coot,
734 while the peripheral U2 snRNP and NTC were improved by applying torsion and distance
735 restraints to reference models produced by AlphaFold2. The model was refined using PHENIX
736 real_space_refine (Liebschner et al., 2019), just performing one macro-cycle. Figures were
737 generated using UCSF ChimeraX.

738 **Plasmid cloning**

739 Fyv6 plasmids were made by PCR amplification from gDNA of the *FYV6* coding sequence
740 plus ~250 nt upstream and downstream, restriction digest with NotI and SalI, and ligation into
741 pRS414 or pRS416. An N-terminal 1x FLAG tag was added onto Fyv6 in the plasmids by PCR
742 mutagenesis. Fyv6 truncations were cloned by Genewiz (Azenta Life Sciences) from pAAH1572.
743 Restriction digest and ligation were used to place Fyv6 constructs into the pRS413 backbone.

744 Syf1 plasmids were made by PCR amplification from gDNA of the SYF1 coding sequence
745 plus ~275 nt upstream and downstream, restriction digest, and ligation into pRS414 or pRS416.

746 Cef1 mutant plasmids, Prp22 I1133R mutant plasmid, Prp8 mutant plasmids, ACT1-CUP1
747 BP-3' SS distance reporters, and Syf1 truncation plasmids were prepared by PCR-based site
748 directed mutagenesis of pAAH1611, pAAH1042, pAAH1440, pAAH0470, and pAAH1625
749 respectively. All plasmids were fully sequenced to confirm their nucleotide sequence.

750 **Yeast strain creation**

751 The *DBR1* and *FYV6* genes were deleted by replacement with a nourseothricin resistance
752 cassette (NatMX4) or hygromycin resistance cassette (hphMX4), respectively, through
753 homologous recombination (see **supplementary table 7**; Goldstein and McCusker, 1999). The
754 *SYF1* and *CEF1* genes were deleted by replacement with a kanamycin resistance cassette
755 (KanMX) through homologous recombination in strains transformed with pRS416-Syf1 or
756 pRS316-Cef1 respectively. Gene deletion was confirmed by colony PCR and/or genomic DNA
757 extraction from the strains and PCR amplification of the corresponding genomic locus.

758 **RNA isolation**

759 Yeast were grown in YPD media until OD_{600} 0.5-0.8. For RNA-sequencing of temperature-
760 shifted samples, cultures were shifted to either 37°C or 16°C or remained at 30°C and grown for
761 1 hr. A 15 mL volume of culture was harvested via vacuum filtration with mixed cellulose ester
762 filter paper (Whatman, 47 mm diameter) in a Buchner funnel. Filter papers were separated into 5
763 mL tubes and flash frozen. Filters were stored at –80°C until RNA isolation. Filters were washed
764 with 1 mL TRIzol to collect cells. For all other experiments involving RNA isolation, 10 OD_{600} units
765 of OD_{600} 0.5-0.8 yeast were harvested via centrifugation.

766 Cell walls were disrupted by incubation with Zymolyase (50 U/mL, Zymo Research) in Y1
767 buffer (1 M sorbitol, 100 mM EDTA pH 8.0, 13 mM β-mercaptoethanol) (primer extension, RNA-
768 seq of non-temperature-shifted samples) or vortexing with silica disruption beads in TRIzol (RT-
769 PCR, RNA-seq of temperature-shifted samples). Total RNA was then isolated using TRIzol
770 reagent (Thermo Fisher Scientific) according to manufacturer's instructions. Samples were
771 cleaned using a 50 µg Monarch RNA Cleanup Kit (New England Biolabs) and treated with TURBO
772 DNase (Thermo Fisher Scientific) to remove residual contaminating DNA. For RNA-sequencing,
773 quality of RNA samples was assessed prior to library preparation by NanoDrop (concentration,
774 A_{260}/A_{280}, and A_{260}/A_{230}), Qubit (RNA High Sensitivity and RNA IQ), and TapeStation (RNA

775 ScreenTape Analysis). High quality samples showing minimal rRNA degradation with RIN >7 and
776 A260/A280 ratios of ~2.0 were selected for library preparation.

777 **Library preparation and RNA sequencing**

778 Library preparation was conducted by the University of Wisconsin-Madison Biotechnology
779 Center Gene Expression Center. mRNA was selected from total RNA samples through polyA
780 enrichment with the TruSeq Stranded mRNA kit (Illumina). Sequencing was performed with an
781 NovaSeq6000 sequencer (Illumina).

782 **Bioinformatic analysis of RNA-seq datasets**

783 FASTQC was used for quality control of reads pre- and post- trimming (Andrews, 2010).
784 Trimming of reads was accomplished using fastp (Chen et al., 2018) prior to mapping to the
785 SacCer3 genome (Ensembl, R64-1-1) with STAR (Dobin et al., 2013). All samples were aligned
786 with STAR in a first pass. Novel junctions from all samples (WT and *fyv6Δ*) were combined and
787 filtered for likely false-positive junctions (see Supplemental Methods). STAR was run in a second
788 pass with the additional input of the filtered set of novel junctions. Indexing of bam files was
789 accomplished with SAMtools (Li et al., 2009). Quantitation of read counts aligned to the SacCer3
790 transcriptome was accomplished with Salmon (Patro et al., 2017). Differential gene expression
791 analysis was conducted with DeSeq2 (Love et al., 2014). Junction reads within genes were
792 counted with featureCounts (Liao et al., 2014) and used to calculate fraction of Annotation Splicing
793 (FAnS) based on methods in Roy et al., 2023 (see Supplemental Methods). Canonical branch
794 points were used as defined in the Ares Intron Database (Grate and Ares, 2002). Differential
795 splicing analysis was conducted with SpliceWiz (Wong et al., 2024).

796 **Primer extension**

797 RNA was isolated using the protocol above. IR700 dye conjugated probes (Integrated DNA
798 Technologies) were used for primer extension with SuperScript III (Thermo Fisher) of the ACT1-
799 CUP1 reporters (2 pmol yAC6: /5IRD700/GGCACTCATGACCTTC) and U6 snRNA (0.4 pmol
800 yU6: /5IRD700/GAACTGCTGATCATGTCTG) (Carrocci et al., 2017; van der Feltz et al., 2021).

801 Primer extension products were visualized on a 7% (w/v) denaturing polyacrylamide gel run at 35
802 W for 80 min at RT. Gels were imaged with an Amersham Typhoon NIR laser scanner (Cytiva),
803 and band intensities were quantified with Image J (version 1.53v, 2022).

804 **RT-PCR**

805 Yeast cultures were inoculated from cultures grown to stationary phase overnight and
806 grown until OD_{600} = 0.7-0.9. RNA was isolated and depleted of contaminating DNA using the
807 MasterPure Yeast RNA Purification Kit (LGC Biosearch Technologies) protocol as previously
808 described (Carrocci et al., 2017) (RT-PCR shown in Fig. 4C) or using the RNA isolation protocol
809 above (all others).

810 RT-PCR reactions were set up using the Access RT-PCR system (Promega Corporation)
811 following the kit procedure with 100 ng of input RNA per 25 µl reaction. Primers to amplify *SUS1*
812 were SUS1-exon1 5'-TGGATACTGCGCAATTAAAGAGTC-3' and SUS1-exon3 5'-
813 TCATTGTGTATCTACAATCTCTTCAAG-3'. Reaction products were separated on 2% (w/v)
814 agarose-TBE gels and imaged using ethidium bromide fluorescence.

815 **Selection of *fyv6Δ* suppressors**

816 Strain yAAH3353 was previously described (Lipinski et al. 2023). Twenty single colonies
817 of yAAH3353 were selected from a YPD plate and used to inoculate 20 x 5mL YPD liquid culture.
818 Cultures were grown for 48 h at 30°C. A 1 mL volume of culture was spun down, resuspended in
819 200 µL YPD liquid medium, and spread on a YPD plate containing 40 mg/L adenine hemisulfate
820 (to prevent ade2 reversion). Duplicate plates for each overnight were placed in incubators at either
821 18°C or 37°C. Many colonies of various sizes appeared on each plate by 9 days for 37°C and 12
822 days for 18°C. Colonies were picked after that time and annotated first by growth temperature,
823 then by overnight number, and finally roughly by colony size with 01 generally being the largest
824 colony on a plate (ex: 370101 from a plate grown at 37°C inoculated from overnight 01 and the
825 largest colony selected from the plate). Picked colonies were grown overnight in 5mL YPD at 30°C

826 and frozen stocks were made. Anywhere from 0 to ~15 colonies were picked per plate, covering
827 the variety of colony sizes that arose.

828 **Sequencing of yeast genomic DNA**

829 Yeast were grown to saturated stationary phase in 5mL YPD and ~10 OD units were sent
830 as a frozen yeast pellet to Azenta or SeqCoast for genomic DNA extraction, library, preparation,
831 and sequencing with 30x/400 mbp coverage.

832 **Bioinformatic analysis of WGS data**

833 Azenta and SeqCoast utilized the SacCer3 genome (Ensembl, R64-1-1) for variant calling
834 and provided a list of >6,000 SNPs. Since the strain is not a perfect match for this reference, non-
835 unique SNPs were filtered from each dataset by taking the union of two sets with each set
836 obtained from colonies isolated on different plates (to reduce the chance of computationally
837 eliminating the same variant SNP). Filtering reduced the dataset to <100 unique variants per
838 colony. Few unique SNPs were within protein- or snRNA-coding genes. Of SNPs within protein-
839 coding regions, single amino acid changes were frequently found within splicing factors (see
840 **Supplemental Table S4**). Datasets were reexamined upon identification of suppressor mutations
841 for suppressor mutation duplication that were potentially filtered out during comparison of SNP
842 datasets.

843 **Yeast temperature growth assays**

844 Yeast were grown to stationary phase overnight in the appropriate liquid medium indicated
845 in the figure legends. The cultures were first diluted to OD_{600} 0.5, serially diluted 1:10, 1:100, and
846 1:1000, and stamped onto agar plates containing the appropriate growth medium. The plates
847 were incubated at 16°, 23°, 30°, and 37°C, and plates were imaged after the number of days
848 indicated in each figure.

849 **ACT1-CUP1 copper tolerance assays**

850 Yeast strains expressing ACT1-CUP1 reporters were grown to stationary phase in -Leu
851 DO media, diluted to OD_{600} = 0.5 in 10% (v/v) glycerol, and spotted onto -Leu DO plates containing

852 0 to 2.5 mM $CuSO_4$ (Lesser and Guthrie 1993; Carrocci et al., 2018). Plates were scored and
853 imaged after 48 h of growth at 30°C for WT strains and after 72 h of growth at 30°C for *fyv6Δ*
854 strains due to differential growth between strains.

855 **Western blotting**

856 Total soluble protein was isolated by TCA precipitation from 10 ODs of an overnight yeast
857 culture. Proteins were separated with a NuPAGE 4 to 12% Bis-Tris pre-cast gel (Invitrogen) using
858 1X NuPAGE MES running buffer (Invitrogen) and transferred to a PVDF membrane (0.2 µm pore
859 size) at 30V for 120 min at 4°C using 1x NuPAGE Transfer Buffer (Invitrogen) with 20% (v/v)
860 methanol in a XCell II Blot Module (Invitrogen). The membrane was blocked with 3% (w/v) BSA
861 (Sigma, A7906) in 1x TBST for 1h at room temperature with gentle shaking. All antibodies were
862 diluted in 1x TBST with 3% (w/v) BSA. The primary antibodies anti-FLAG (Millipore Sigma, F1804;
863 diluted 1:1000) and anti-actin (Sigma Aldrich, MAB1501; diluted 1:5000) were incubated overnight
864 at 4°C. The membrane was then washed with 1x TBST before incubation with goat anti-mouse
865 IgG HRP conjugate secondary antibody (Biorad, #1706516; diluted 1:8000) for 2h at room
866 temperature. The membrane was then washed with 1x TBST before developing with Clarity
867 Western ECL substrate (Biorad, #1705060) with a 20s exposure for anti-actin and a 100s
868 exposure for anti-FLAG.

869

870 **ACKNOWLEDGEMENTS**

871 We thank David Brow for his advice on the suppressor screen. We thank Justin Mabin for
872 his advice on RNA-sequencing data analysis. MEW is grateful to Feng Zhang for funding and
873 support, and to the labs of Kiyoshi Nagai and Kelly Nguyen for reagents and support. The authors
874 utilized the University of Wisconsin – Madison Biotechnology Center Gene Expression Center
875 (Research Resource Identifier – RRID:SCR_017757) for preparation of NGS libraries for RNA-
876 sequencing and the Biochemistry Computational Research Facility (BCRF) for analysis of RNA-
877 sequencing datasets. This work was supported by grants from the National Institutes of Health

878 (R35 GM136261 to AAH), NIH Biotechnology Training Program (T32 GM135066) and National
879 Science Foundation Graduate Research Fellowship Program (Grant No. DGE-1747503)
880 fellowships to KAS, a Helen Hay Whitney Postdoctoral Fellowship (to MEW). This study was
881 supported by the MRC Laboratory of Molecular Biology electron microscopy facility. We thank
882 Guillaume Chanfreau for advice and Florian Heyd and Tucker Carrocci for critical reading of the
883 manuscript.

884

885 **CONTRIBUTIONS**

886 AAH, KAS, KAL, and MEW conceptualized the project; MEW collected and analyzed the cryo-EM
887 data; KAL and NJZ prepared RNA for sequencing; KAL, NJZ, and AFG analyzed the RNA-
888 sequencing data; AAH, KAS, NJZ, and KAL created yeast strains; KAS, KAL, NJZ, and AFG
889 performed genetic and biochemical assays and analyzed data; KAS, KAL, MEW, and AAH wrote
890 the manuscript.

891

892 **DATA AND MATERIALS AVAILABILITY**

893 RNA-seq data has been uploaded to NCBI SRA with BioProject ID PRJNA1113593. R code for
894 calculation of FAnS values can be found at the following DOI: 10.5281/zenodo.13798743. The
895 cryo-EM maps and atomic model of the P complex (state I) have been deposited in the Electron
896 Microscopy Data Bank (https://www.ebi.ac.uk/pdbe/emdb/) and in the Protein Data Bank
897 (https://www.rcsb.org). The data are available under the following accession codes: P complex
898 state I (EMD-47157, EMD-47160, EMD-47161, EMD-47162, EMD47163, EMD-47164; PDB
899 9DTR), state II (EMD-47158), and state III (EMD-47159). Raw cryo-EM data is available from
900 EMPIAR (EMPIAR-12330).

901

902 **COMPETING INTEREST STATEMENT**

AAH is a member of the scientific advisory board and carrying out sponsored research for Remix Therapeutics.

REFERENCES

Andrews, S. (2010). *FastQC: a quality control tool for high throughput sequence data* [Computer software]. http://www.bioinformatics.babraham.ac.uk/projects/fastqc

Aronova, A., Bacíková, D., Crotti, L. B., Horowitz, D. S., & Schwer, B. (2007). Functional interactions between Prp8, Prp18, Slu7, and U5 snRNA during the second step of pre-mRNA splicing. *RNA*, *13*(9), 1437–1444. https://doi.org/10.1261/rna.572807

Bai, R., Yan, C., Wan, R., Lei, J., & Shi, Y. (2017). Structure of the Post-catalytic Spliceosome from Saccharomyces cerevisiae. *Cell*, *171*(7), 1589-1598.e8. https://doi.org/10.1016/j.cell.2017.10.038

Bepler, T., Morin, A., Rapp, M., Brasch, J., Shapiro, L., Noble, A. J., & Berger, B. (2019). Positive-unlabeled convolutional neural networks for particle picking in cryo-electron micrographs. *Nature Methods*, *16*(11), Article 11. https://doi.org/10.1038/s41592-019-0575-8

Brow, D. A. (2019). An Allosteric Network for Spliceosome Activation Revealed by High-Throughput Suppressor Analysis in Saccharomyces cerevisiae. *Genetics*, *212*(1), 111–124. https://doi.org/10.1534/genetics.119.301922

Brys, A., & Schwer, B. (1996). Requirement for SLU7 in yeast pre-mRNA splicing is dictated by the distance between the branchpoint and the 3' splice site. *RNA*, *2*(7), 707–717.

Carrocci, T. J., Paulson, J. C., & Hoskins, A. A. (2018). Functional analysis of Hsh155/SF3b1 interactions with the U2 snRNA/branch site duplex. *RNA*, *24*(8), 1028–1040. https://doi.org/10.1261/rna.065664.118

Carrocci, T. J., Zoerner, D. M., Paulson, J. C., & Hoskins, A. A. (2017). SF3b1 mutations associated with myelodysplastic syndromes alter the fidelity of branchsite selection in yeast. *Nucleic Acids Research*, *45*(8), 4837–4852. https://doi.org/10.1093/nar/gkw1349

Casañal, A., Lohkamp, B., & Emsley, P. (2020). Current developments in Coot for macromolecular model building of Electron Cryo-microscopy and Crystallographic Data. *Protein Science*, *29*(4), 1055–1064. https://doi.org/10.1002/pro.3791

Chen, C.-H., Tsai, W.-Y., Chen, H.-R., Wang, C.-H., & Cheng, S.-C. (2001). Identification and Characterization of Two Novel Components of The Prp19p-associated Complex, Ntc30p and Ntc20p *. *Journal of Biological Chemistry*, *276*(1), 488–494. https://doi.org/10.1074/jbc.M006958200

Chen, S., Zhou, Y., Chen, Y., & Gu, J. (2018). fastp: An ultra-fast all-in-one FASTQ preprocessor. *Bioinformatics*, *34*(17), i884–i890. https://doi.org/10.1093/bioinformatics/bty560

Chiang, T.-W., & Cheng, S.-C. (2013). A Weak Spliceosome-Binding Domain of Yju2 Functions in the First Step and Bypasses Prp16 in the Second Step of Splicing. *Molecular and Cellular Biology*, *33*(9), 1746–1755. https://doi.org/10.1128/MCB.00035-13

Chua, K., & Reed, R. (1999). The RNA splicing factor hSlu7 is required for correct 3′ splice-site choice. *Nature*, *402*(6758), 207–210. https://doi.org/10.1038/46086

Chung, C.-S., Wai, H. L., Kao, C.-Y., & Cheng, S.-C. (2023). An ATP-independent role for Prp16 in promoting aberrant splicing. *Nucleic Acids Research*, *51*(20), 10815–10828. https://doi.org/10.1093/nar/gkad861

Chung, S., McLean, M. R., & Rymond, B. C. (1999). Yeast ortholog of the Drosophila crooked neck protein promotes spliceosome assembly through stable U4/U6.U5 snRNP addition. *RNA*, *5*(8), 1042–1054.

Company, M., Arenas, J., & Abelson, J. (1991). Requirement of the RNA helicase-like protein PRP22 for release of messenger RNA from spliceosomes. *Nature*, *349*(6309), 487–493. https://doi.org/10.1038/349487a0

Corvelo, A., Hallegger, M., Smith, C. W. J., & Eyras, E. (2010). Genome-Wide Association between Branch Point Properties and Alternative Splicing. *PLOS Computational Biology*, *6*(11), e1001016. https://doi.org/10.1371/journal.pcbi.1001016

Croll, T. I. (2018). ISOLDE: A physically realistic environment for model building into low-resolution electron-density maps. *Acta Crystallographica Section D: Structural Biology*, *74*(6), 519–530. https://doi.org/10.1107/S2059798318002425

Crotti, L. B., Bačíková, D., & Horowitz, D. S. (2007). The Prp18 protein stabilizes the interaction of both exons with the U5 snRNA during the second step of pre-mRNA splicing. *Genes & Development*, *21*(10), 1204–1216. https://doi.org/10.1101/gad.1538207

Dobin, A., Davis, C. A., Schlesinger, F., Drenkow, J., Zaleski, C., Jha, S., Batut, P., Chaisson, M., & Gingeras, T. R. (2013). STAR: Ultrafast universal RNA-seq aligner. *Bioinformatics*, *29*(1), 15–21. https://doi.org/10.1093/bioinformatics/bts635

Felisberto-Rodrigues, C., Thomas, J. C., McAndrew, C., Le Bihan, Y.-V., Burke, R., Workman, P., & van Montfort, R. L. M. (2019). Structural and functional characterisation of human RNA helicase DHX8 provides insights into the mechanism of RNA-stimulated ADP release. *Biochemical Journal*, *476*(18), 2521–2543. https://doi.org/10.1042/BCJ20190383

Feltz, C. van der, Nikolai, B., Schneider, C., Paulson, J. C., Fu, X., & Hoskins, A. A. (2021). Saccharomyces cerevisiae Ecm2 modulates the catalytic steps of pre-mRNA splicing. *RNA*, *27*(5), 591–603. https://doi.org/10.1261/rna.077727.120

Fica, S. M., & Nagai, K. (2017). Cryo-electron microscopy snapshots of the spliceosome: Structural insights into a dynamic ribonucleoprotein machine. *Nature Structural & Molecular Biology*, *24*(10), Article 10. https://doi.org/10.1038/nsmb.3463

Fica, S. M., Oubridge, C., Wilkinson, M. E., Newman, A. J., & Nagai, K. (2019). A human postcatalytic spliceosome structure reveals essential roles of metazoan factors for exon ligation. *Science*, *363*(6428), 710–714. https://doi.org/10.1126/science.aaw5569

Frank, D., & Guthrie, C. (1992). An essential splicing factor, SLU7, mediates 3’ splice site choice in yeast. *Genes & Development*, *6*(11), 2112–2124. https://doi.org/10.1101/gad.6.11.2112

Galej, W. P., Oubridge, C., Newman, A. J., & Nagai, K. (2013). Crystal structure of Prp8 reveals active site cavity of the spliceosome. *Nature*, *493*(7434), 638–643. https://doi.org/10.1038/nature11843

Gautam, A., Grainger, R. J., Vilardell, J., Barrass, J. D., & Beggs, J. D. (2015). Cwc21p promotes the second step conformation of the spliceosome and modulates 3′ splice site selection. *Nucleic Acids Research*, *43*(6), 3309–3317. https://doi.org/10.1093/nar/gkv159

Goldstein, A. L., & McCusker, J. H. (1999). Three new dominant drug resistance cassettes for gene disruption in Saccharomyces cerevisiae. *Yeast*, *15*(14), 1541–1553. https://doi.org/10.1002/(SICI)1097-0061(199910)15:14<1541::AID-YEA476>3.0.CO;2-K

Gooding, C., Clark, F., Wollerton, M. C., Grellscheid, S.-N., Groom, H., & Smith, C. W. (2006). A class of human exons with predicted distant branch points revealed by analysis of AG dinucleotide exclusion zones. *Genome Biology*, *7*(1), R1. https://doi.org/10.1186/gb-2006-7-1-r1

Grate, L., & Ares, M. (2002). Searching yeast intron data at ares lab web site. In C. Guthrie & G. R. Fink (Eds.), *Methods in Enzymology* (Vol. 350, pp. 380–392). Academic Press. https://doi.org/10.1016/S0076-6879(02)50975-7

Hossain, M. A., Claggett, J. M., Nguyen, T., & Johnson, T. L. (2009). The cap binding complex influences H2B ubiquitination by facilitating splicing of the SUS1 pre-mRNA. *RNA*, *15*(8), 1515–1527. https://doi.org/10.1261/rna.1540409

Kawashima, T., Douglass, S., Gabunilas, J., Pellegrini, M., & Chanfreau, G. F. (2014). Widespread Use of Non-productive Alternative Splice Sites in Saccharomyces cerevisiae. *PLOS Genetics*, *10*(4), e1004249. https://doi.org/10.1371/journal.pgen.1004249

Kimanius, D., Jamali, K., Wilkinson, M. E., Lövestam, S., Velazhahan, V., Nakane, T., & Scheres, S. H. W. (2024). Data-driven regularization lowers the size barrier of cryo-EM structure determination. *Nature Methods*, *21*(7), 1216–1221. https://doi.org/10.1038/s41592-024-02304-8

Koodathingal, P., Novak, T., Piccirilli, J. A., & Staley, J. P. (2010). The DEAH Box ATPases Prp16 and Prp43 Cooperate to Proofread 5′ Splice Site Cleavage during Pre-mRNA Splicing. *Molecular Cell*, *39*(3), 385–395. https://doi.org/10.1016/j.molcel.2010.07.014

Kuhn, A. N., & Brow, D. A. (2000). Suppressors of a Cold-Sensitive Mutation in Yeast U4 RNA Define Five Domains in the Splicing Factor Prp8 That Influence Spliceosome Activation. *Genetics*, *155*(4), 1667–1682. https://doi.org/10.1093/genetics/155.4.1667

Kuhn, A. N., Li, Z., & Brow, D. A. (1999). Splicing Factor Prp8 Governs U4/U6 RNA Unwinding during Activation of the Spliceosome. *Molecular Cell*, *3*(1), 65–75. https://doi.org/10.1016/S1097-2765(00)80175-6

Lesser, C. F., & Guthrie, C. (1993). Mutational analysis of pre-mRNA splicing in Saccharomyces cerevisiae using a sensitive new reporter gene, CUP1. *Genetics*, *133*(4), 851–863. https://doi.org/10.1093/genetics/133.4.851

Li, H., Handsaker, B., Wysoker, A., Fennell, T., Ruan, J., Homer, N., Marth, G., Abecasis, G., Durbin, R., & 1000 Genome Project Data Processing Subgroup. (2009). The Sequence Alignment/Map format and SAMtools. *Bioinformatics*, *25*(16), 2078–2079. https://doi.org/10.1093/bioinformatics/btp352

1028 Liang, W.-W., & Cheng, S.-C. (2015). A novel mechanism for Prp5 function in prespliceosome
1029 formation and proofreading the branch site sequence. *Genes & Development*, *29*(1), 81–
1030 93. https://doi.org/10.1101/gad.253708.114

1031 Liao, Y., Smyth, G. K., & Shi, W. (2014). featureCounts: An efficient general purpose program for
1032 assigning sequence reads to genomic features. *Bioinformatics*, *30*(7), 923–930.
1033 https://doi.org/10.1093/bioinformatics/btt656

1034 Liebschner, D., Afonine, P. V., Baker, M. L., Bunkóczi, G., Chen, V. B., Croll, T. I., Hintze, B.,
1035 Hung, L. W., Jain, S., McCoy, A. J., Moriarty, N. W., Oeffner, R. D., Poon, B. K., Prisant,
1036 M. G., Read, R. J., Richardson, J. S., Richardson, D. C., Sammito, M. D., Sobolev, O. V.,
1037 … Adams, P. D. (2019). Macromolecular structure determination using X-rays, neutrons
1038 and electrons: Recent developments in Phenix. *Acta Crystallographica. Section D,*
1039 *Structural Biology*, *75*(Pt 10), 861–877. https://doi.org/10.1107/S2059798319011471

1040 Lin, R. J., Newman, A. J., Cheng, S. C., & Abelson, J. (1985). Yeast mRNA splicing in vitro.
1041 *Journal of Biological Chemistry*, *260*(27), 14780–14792. https://doi.org/10.1016/S0021-
1042 9258(17)38641-6

1043 Lipinski, K. A., Senn, K. A., Zeps, N. J., & Hoskins, A. A. (2023). Biochemical and Genetic
1044 Evidence Supports Fyv6 as a Second-Step Splicing Factor in Saccharomyces
1045 cerevisiae. *RNA*, rna.079607.123. https://doi.org/10.1261/rna.079607.123

1046 Liu, L., Query, C. C., & Konarska, M. M. (2007). Opposing classes of prp8 alleles modulate the
1047 transition between the catalytic steps of pre-mRNA splicing. *Nature Structural &*
1048 *Molecular Biology*, *14*(6), Article 6. https://doi.org/10.1038/nsmb1240

1049 Liu, S., Li, X., Zhang, L., Jiang, J., Hill, R. C., Cui, Y., Hansen, K. C., Zhou, Z. H., & Zhao, R.
1050 (2017). Structure of the yeast spliceosomal postcatalytic P complex. *Science*, *358*(6368),
1051 Article 6368. https://doi.org/10.1126/science.aar3462

1052 Liu, Y.-C., Chen, H.-C., Wu, N.-Y., & Cheng, S.-C. (2007). A Novel Splicing Factor, Yju2, Is
1053 Associated with NTC and Acts after Prp2 in Promoting the First Catalytic Reaction of
1054 Pre-mRNA Splicing. *Molecular and Cellular Biology*, *27*(15), 5403–5413.
1055 https://doi.org/10.1128/MCB.00346-07

1056 Love, M. I., Huber, W., & Anders, S. (2014). Moderated estimation of fold change and dispersion
1057 for RNA-seq data with DESeq2. *Genome Biology*, *15*(12), 550.
1058 https://doi.org/10.1186/s13059-014-0550-8

1059 Mayas, R. M., Maita, H., & Staley, J. P. (2006). Exon ligation is proofread by the DExD/H-box
1060 ATPase Prp22p. *Nature Structural & Molecular Biology*, *13*(6), Article 6.
1061 https://doi.org/10.1038/nsmb1093

1062 McPheeters, D. S., & Abelson, J. (1992). Mutational analysis of the yeast U2 snRNA suggests a
1063 structural similarity to the catalytic core of group I introns. *Cell*, *71*(5), 819–831.
1064 https://doi.org/10.1016/0092-8674(92)90557-s

1065 Mendoza-Ochoa, G. I., Barrass, J. D., Maudlin, I. E., & Beggs, J. D. (2019). Blocking late stages
1066 of splicing quickly limits pre-spliceosome assembly in vivo. *RNA Biology*, *16*(12), 1775–
1067 1784. https://doi.org/10.1080/15476286.2019.1657788

1068 Montemayor, E. J., Curran, E. C., Liao, H. H., Andrews, K. L., Treba, C. N., Butcher, S. E., &
1069 Brow, D. A. (2014). Core structure of the U6 small nuclear ribonucleoprotein at 1.7-Å
1070 resolution. *Nature Structural & Molecular Biology*, *21*(6), Article 6.
1071 https://doi.org/10.1038/nsmb.2832

1072 Mumberg, D., Müller, R., & Funk, M. (1995). Yeast vectors for the controlled expression of
1073 heterologous proteins in different genetic backgrounds. *Gene*, *156*(1), 119–122.
1074 https://doi.org/10.1016/0378-1119(95)00037-7

1075 Munding, E. M., Shiue, L., Katzman, S., Donohue, J. P., & Ares, M. (2013). Competition
1076 between Pre-mRNAs for the Splicing Machinery Drives Global Regulation of Splicing.
1077 *Molecular Cell*, *51*(3), 338–348. https://doi.org/10.1016/j.molcel.2013.06.012

1078 Nguyen Ba, A. N., Pogoutse, A., Provart, N., & Moses, A. M. (2009). NLStradamus: A simple
1079 Hidden Markov Model for nuclear localization signal prediction. *BMC Bioinformatics*,
1080 *10*(1), 202. https://doi.org/10.1186/1471-2105-10-202

1081 Patro, R., Duggal, G., Love, M. I., Irizarry, R. A., & Kingsford, C. (2017). Salmon provides fast
1082 and bias-aware quantification of transcript expression. *Nature Methods*, *14*(4), 417–419.
1083 https://doi.org/10.1038/nmeth.4197

1084 Perriman, R., Barta, I., Voeltz, G. K., Abelson, J., & Ares, M. (2003). ATP requirement for Prp5p
1085 function is determined by Cus2p and the structure of U2 small nuclear RNA.
1086 *Proceedings of the National Academy of Sciences*, *100*(24), 13857–13862.
1087 https://doi.org/10.1073/pnas.2036312100

1088 Pettersen, E. F., Goddard, T. D., Huang, C. C., Meng, E. C., Couch, G. S., Croll, T. I., Morris, J.
1089 H., & Ferrin, T. E. (2021). UCSF ChimeraX: Structure visualization for researchers,
1090 educators, and developers. *Protein Science*, *30*(1), 70–82.
1091 https://doi.org/10.1002/pro.3943
1092
1093 Plaschka, C., Newman, A. J., & Nagai, K. (2019). Structural Basis of Nuclear pre-mRNA
1094 Splicing: Lessons from Yeast. *Cold Spring Harbor Perspectives in Biology*, *11*(5),
1095 a032391. https://doi.org/10.1101/cshperspect.a032391

1096 Query, C. C., & Konarska, M. M. (2004). Suppression of Multiple Substrate Mutations by
1097 Spliceosomal prp8 Alleles Suggests Functional Correlations with Ribosomal Ambiguity
1098 Mutants. *Molecular Cell*, *14*(3), 343–354. https://doi.org/10.1016/S1097-2765(04)00217-
1099 5

1100 Query, C. C., & Konarska, M. M. (2012). CEF1/CDC5 alleles modulate transitions between
1101 catalytic conformations of the spliceosome. *RNA*, *18*(5), 1001–1013.
1102 https://doi.org/10.1261/rna.029421.111

1103 Roy, K. R., Gabunilas, J., Neutel, D., Ai, M., Yeh, Z., Samson, J., Lyu, G., & Chanfreau, G. F.
1104 (2023). Splicing factor Prp18p promotes genome-wide fidelity of consensus 3′-splice
1105 sites. *Nucleic Acids Research*, gkad968. https://doi.org/10.1093/nar/gkad968

1106 Sayani, S., Janis, M., Lee, C. Y., Toesca, I., & Chanfreau, G. F. (2008). Widespread Impact of
1107 Nonsense-Mediated mRNA Decay on the Yeast Intronome. *Molecular Cell*, *31*(3), 360–
1108 370. https://doi.org/10.1016/j.molcel.2008.07.005

1109 Schneider, C. A., Rasband, W. S., & Eliceiri, K. W. (2012). NIH Image to ImageJ: 25 years of
1110 image analysis. *Nature Methods*, *9*(7), 671–675. https://doi.org/10.1038/nmeth.2089
1111
1112 Schwer, B. (2008). A Conformational Rearrangement in the Spliceosome Sets the Stage for
1113 Prp22-Dependent mRNA Release. *Molecular Cell*, *30*(6), Article 6.
1114 https://doi.org/10.1016/j.molcel.2008.05.003

1115 Schwer, B., & Gross, C. H. (1998). Prp22, a DExH-box RNA helicase, plays two distinct roles in
1116 yeast pre-mRNA splicing. *The EMBO Journal*, *17*(7), 2086–2094.
1117 https://doi.org/10.1093/emboj/17.7.2086

Schwer, B., & Guthrie, C. (1992). A conformational rearrangement in the spliceosome is dependent on PRP16 and ATP hydrolysis. *The EMBO Journal*, *11*(13), 5033–5039. https://doi.org/10.1002/j.1460-2075.1992.tb05610.x

Schwer, B., & Meszaros, T. (2000). RNA helicase dynamics in pre-mRNA splicing. *The EMBO Journal*, *19*(23), 6582–6591. https://doi.org/10.1093/emboj/19.23.6582

Semlow, D. R., Blanco, M. R., Walter, N. G., & Staley, J. P. (2016). Spliceosomal DEAH-Box ATPases Remodel Pre-mRNA to Activate Alternative Splice Sites. *Cell*, *164*(5), Article 5. https://doi.org/10.1016/j.cell.2016.01.025

Semlow, D. R., & Staley, J. P. (2012). Staying on message: Ensuring fidelity in pre-mRNA splicing. *Trends in Biochemical Sciences*, *37*(7), 263–273. https://doi.org/10.1016/j.tibs.2012.04.001

Siatecka, M., Reyes, J. L., & Konarska, M. M. (1999). Functional interactions of Prp8 with both splice sites at the spliceosomal catalytic center. *Genes & Development*, *13*(15), 1983–1993.

Sikorski, R. S., & Boeke, J. D. (1991). In Vitro Mutagenesis and Plasmid Shuffling: From Cloned Gene to Mutant Yeast. *Methods in Enzymology*, *194*(C), 302–318. https://doi.org/10.1016/0076-6879(91)94023-6

Strittmatter, L. M., Capitanchik, C., Newman, A. J., Hallegger, M., Norman, C. M., Fica, S. M., Oubridge, C., Luscombe, N. M., Ule, J., & Nagai, K. (2021). psiCLIP reveals dynamic RNA binding by DEAH-box helicases before and after exon ligation. *Nature Communications*, *12*(1), 1488. https://doi.org/10.1038/s41467-021-21745-9

Talkish, J., Igel, H., Hunter, O., Horner, S. W., Jeffery, N. N., Leach, J. R., Jenkins, J. L., Kielkopf, C. L., & Ares, M. (2019). Cus2 enforces the first ATP-dependent step of splicing by binding to yeast SF3b1 through a UHM–ULM interaction. *RNA*, *25*(8), 1020–1037. https://doi.org/10.1261/rna.070649.119

Townsend, C., Leelaram, M. N., Agafonov, D. E., Dybkov, O., Will, C. L., Bertram, K., Urlaub, H., Kastner, B., Stark, H., & Lührmann, R. (2020). Mechanism of protein-guided folding of the active site U2/U6 RNA during spliceosome activation. *Science*, *370*(6523), eabc3753. https://doi.org/10.1126/science.abc3753

Treco, D. A., & Lundblad, V. (1993). Preparation of Yeast Media. *Current Protocols in Molecular Biology*, *23*(1), 13.1.1-13.1.7. https://doi.org/10.1002/0471142727.mb1301s23

Vorländer, M. K., Rothe, P., Kleifeld, J., Cormack, E. D., Veleti, L., Riabov-Bassat, D., Fin, L., Phillips, A. W., Cochella, L., & Plaschka, C. (2024). Mechanism for the initiation of spliceosome disassembly. *Nature*, *632*(8024), 443–450. https://doi.org/10.1038/s41586-024-07741-1

Wan, R., Yan, C., Bai, R., Lei, J., & Shi, Y. (2017). Structure of an Intron Lariat Spliceosome from Saccharomyces cerevisiae. *Cell*, *171*(1), 120-132.e12. https://doi.org/10.1016/j.cell.2017.08.029

Wilkinson, M. E., Fica, S. M., Galej, W. P., & Nagai, K. (2021). Structural basis for conformational equilibrium of the catalytic spliceosome. *Molecular Cell*. https://doi.org/10.1016/j.molcel.2021.02.021

Wilkinson, M. E., Fica, S. M., Galej, W. P., Norman, C. M., Newman, A. J., & Nagai, K. (2017). Postcatalytic spliceosome structure reveals mechanism of 3′–splice site selection. *Science*, *358*(6368), 1283–1288. https://doi.org/10.1126/science.aar3729

Wilkinson, M. E., Kumar, A., & Casañal, A. (2019). Methods for merging data sets in electron cryo-microscopy. *Acta Crystallographica Section D: Structural Biology*, *75*(9), 782–791. https://doi.org/10.1107/S2059798319010519

Wong, A. C. H., Wong, J. J.-L., Rasko, J. E. J., & Schmitz, U. (2024). SpliceWiz: Interactive analysis and visualization of alternative splicing in R. *Briefings in Bioinformatics*, *25*(1), bbad468. https://doi.org/10.1093/bib/bbad468

Wu, T., Ruan, K., & Liu, W. (1996). A Fluorescence-Labeling Method for Sequencing Small RNA on Polyacrylamide Gel. *Nucleic Acids Research*, *24*(17), 3472–3473. https://doi.org/10.1093/nar/24.17.3472

Xu, Y.-Z., & Query, C. C. (2007). Competition between the ATPase Prp5 and Branch Region-U2 snRNA Pairing Modulates the Fidelity of Spliceosome Assembly. *Molecular Cell*, *28*(5), 838–849. https://doi.org/10.1016/j.molcel.2007.09.022

Yan, C., Hang, J., Wan, R., Huang, M., Wong, C. C. L., & Shi, Y. (2015). Structure of a yeast spliceosome at 3.6-angstrom resolution. *Science*, *349*(6253), 1182–1191. https://doi.org/10.1126/science.aac7629

Yan, D., Perriman, R., Igel, H., Howe, K. J., Neville, M., & Ares Jr., M. (1998). CUS2, a Yeast Homolog of Human Tat-SF1, Rescues Function of Misfolded U2 through an Unusual RNA Recognition Motif. *Molecular and Cellular Biology*, *18*(9), 5000–5009. https://doi.org/10.1128/MCB.18.9.5000

Zhan, X., Lu, Y., Zhang, X., Yan, C., & Shi, Y. (2022). Mechanism of exon ligation by human spliceosome. *Molecular Cell*, *82*(15), Article 15. https://doi.org/10.1016/j.molcel.2022.05.021

Zhang, X., & Schwer, B. (1997). Functional and physical interaction between the yeast splicing factors Slu7 and Prp18. *Nucleic Acids Research*, *25*(11), 2146–2152. https://doi.org/10.1093/nar/25.11.2146

Zhang, X., Zhan, X., Yan, C., Zhang, W., Liu, D., Lei, J., & Shi, Y. (2019). Structures of the human spliceosomes before and after release of the ligated exon. *Cell Research*, *29*(4), Article 4. https://doi.org/10.1038/s41422-019-0143-x

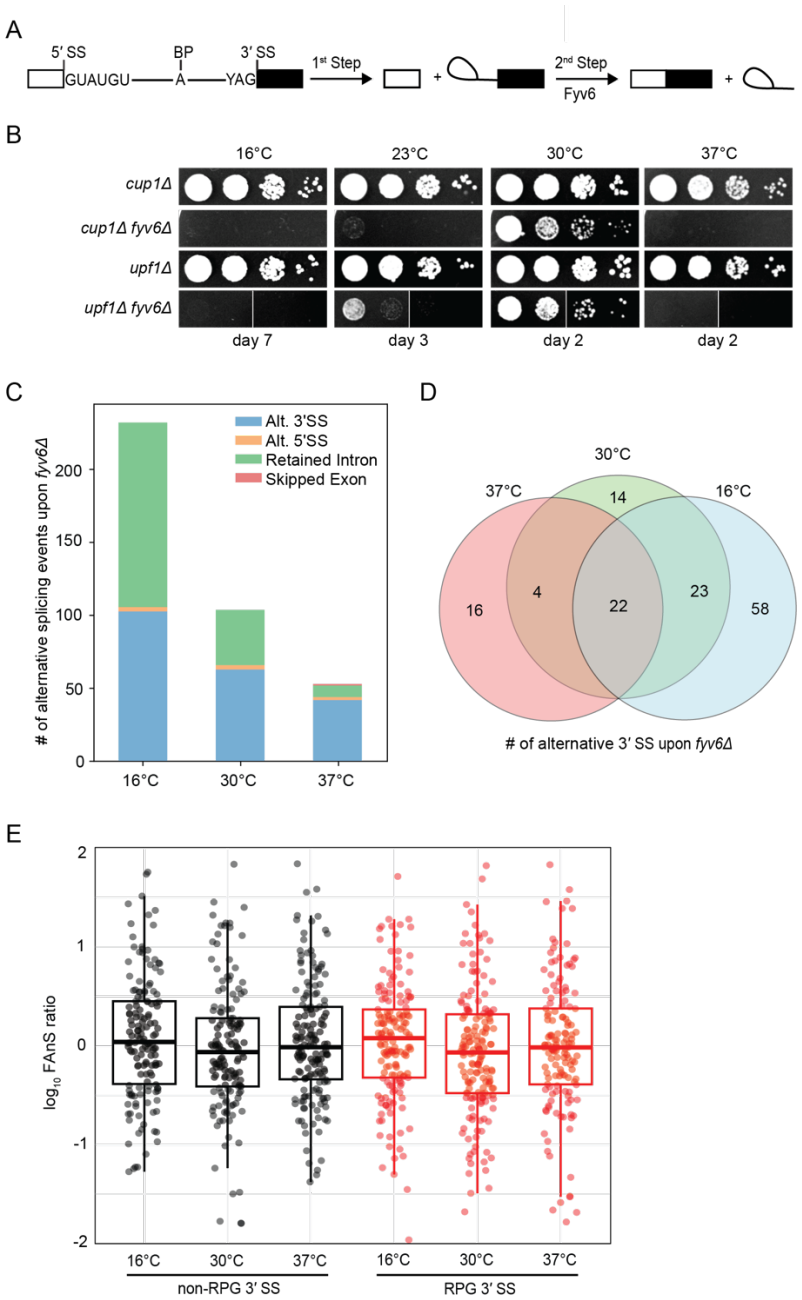

Figure 1. Widespread splicing changes due to loss of Fyv6. A) Pre-mRNA splicing reaction steps and products. **B)** Growth of WT (*cup1Δ*), *fyv6Δ*, *upf1Δ* and *fyv6Δupf1Δ* yeast at 16, 23, 30, and 37°C. Images were taken on the indicated days. White lines indicate where images were cropped, as all dilutions for all strains were on the same plate, but not necessarily directly adjacent to one another. **C)** Number of alternative splicing events observed in a *fyv6Δupf1Δ* strain relative to a strain containing FYV6 after a temperature shift to 16, 30, and 37°C. **D)** Venn diagram of shared alternative 3′ SS splicing events at 16 (blue), 30 (green), and 37°C (red). **E)** Box plots of the $\log_{10}$ of the ratios of *fyv6Δ upf1Δ* to WT (*upf1Δ*) Fraction of Annotated Splicing (FAnS) values for RPGs (red) and non-RPGs (black) for 3′ SS splicing events. FAnS values represent the ratio of the alternative splicing event (here, selection of an alternate 3′ SS) to the annotated, canonical splice isoform.

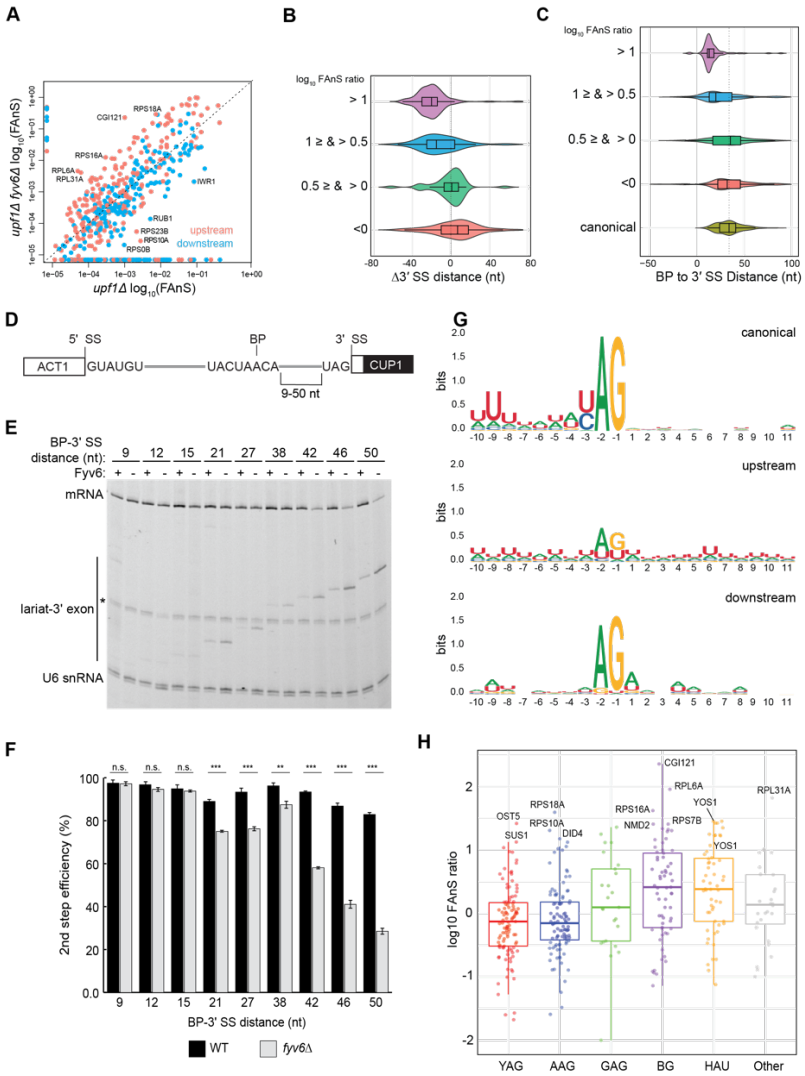

Figure 2: Loss of Fyv6 activates BP proximal, non-consensus 3' SS. A) Plot of the $\log_{10}$ of Fraction of Annotated Splicing (FAnS) values for differences between alternative 3' SS usage in *fyv6Δ upf1Δ* and *upf1Δ* strains. High FAnS values indicate increased usage of the alternate 3' SS relative to the annotated site. Points are colored based on whether they are upstream (pink) or downstream (blue) to the canonical 3' SS. **B)** Violin plots of the ratios of *fyv6Δupf1Δ* to the *upf1Δ* FAnS values based on the distances between the alternative and canonical 3' SS (Δ3' SS = 3' $SS_{Alt.}$ - 3' $SS_{canonical}$). FAnS ratios >0 are indicative of the site being upregulated in *fyv6Δ*. **C)** Violin plots of the ratios of *fyv6Δupf1Δ* to the *upf1Δ* FAnS values based on the distances between the alternative 3' SS and the annotated BP. FAnS ratios >0 are indicative of the site being upregulated in *fyv6Δ*. **D)** Diagram of ACT1-CUP1 reporter showing BP-3' SS distances. **E)** Representative primer extension analysis of RNA products generated from splicing of the ACT1-CUP1 reporter in the presence (WT) or absence of Fyv6 (*fyv6Δ*). Bands for fully spliced mRNA and lariat intermediate are indicated. U6 snRNA was detected as a loading control. The * indicates an unknown product present in every lane. **F)** Quantification of the primer extension results from *N*=3 replicates represented by the ratio of band intensities for mRNA/(mRNA+lariat intermediate). Bars represent the average ratio of the replicates ±SD. Means between WT and *fyv6Δ* groups for each reporter were compared with an unpaired Welch's two-tailed t-test. Significance is indicated: n.s. no significance; ** $p<0.01$; *** $p<0.001$. **G)** Sequence logos of

alternative 3' SS with FAnS > 0 sorted by either upstream or downstream of the canonical 3' SS compared against the canonical 3' SS for genes with FAnS > 0. **H)** The $\log_{10}$ of the FAnS ratio for alternative 3' SS sorted by the sequences of the 3' SS.

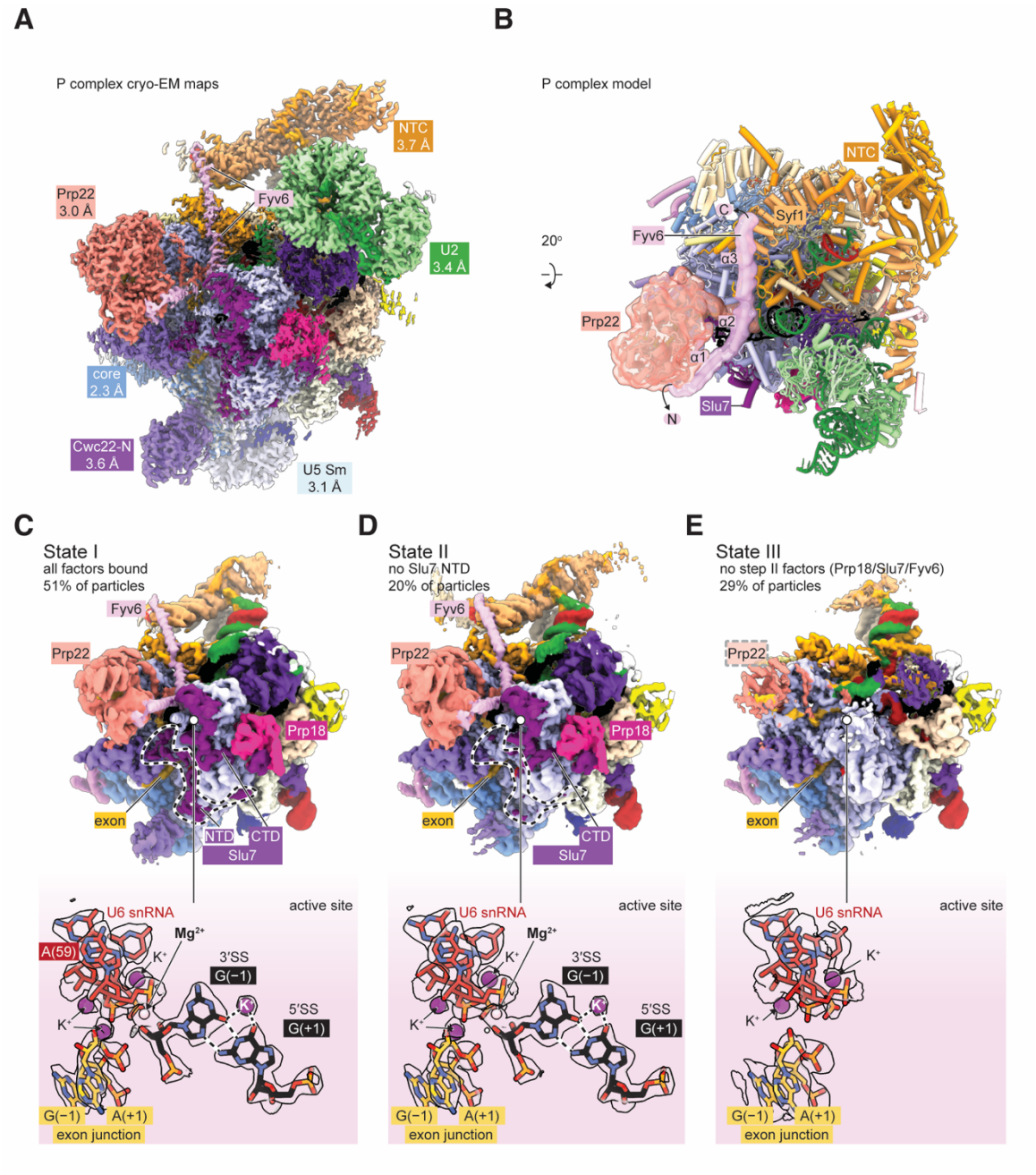

Figure 3. Cryo-EM structure of the yeast P complex spliceosome at 2.3 Å resolution. A) A composite density map for P complex showing focused refinements of the Prp22, NTC, U2 snRNP, U5 Sm ring, and Cwc22 N-terminal domain regions. **B)** Overall model for the P complex spliceosome. **C)** Cryo-EM density for state I of P complex (above, low-pass filtered) and for the active site and 3' SS (below, sharpened). **D,E**) As for **C)** but for states II (**D**) and III (**E**).

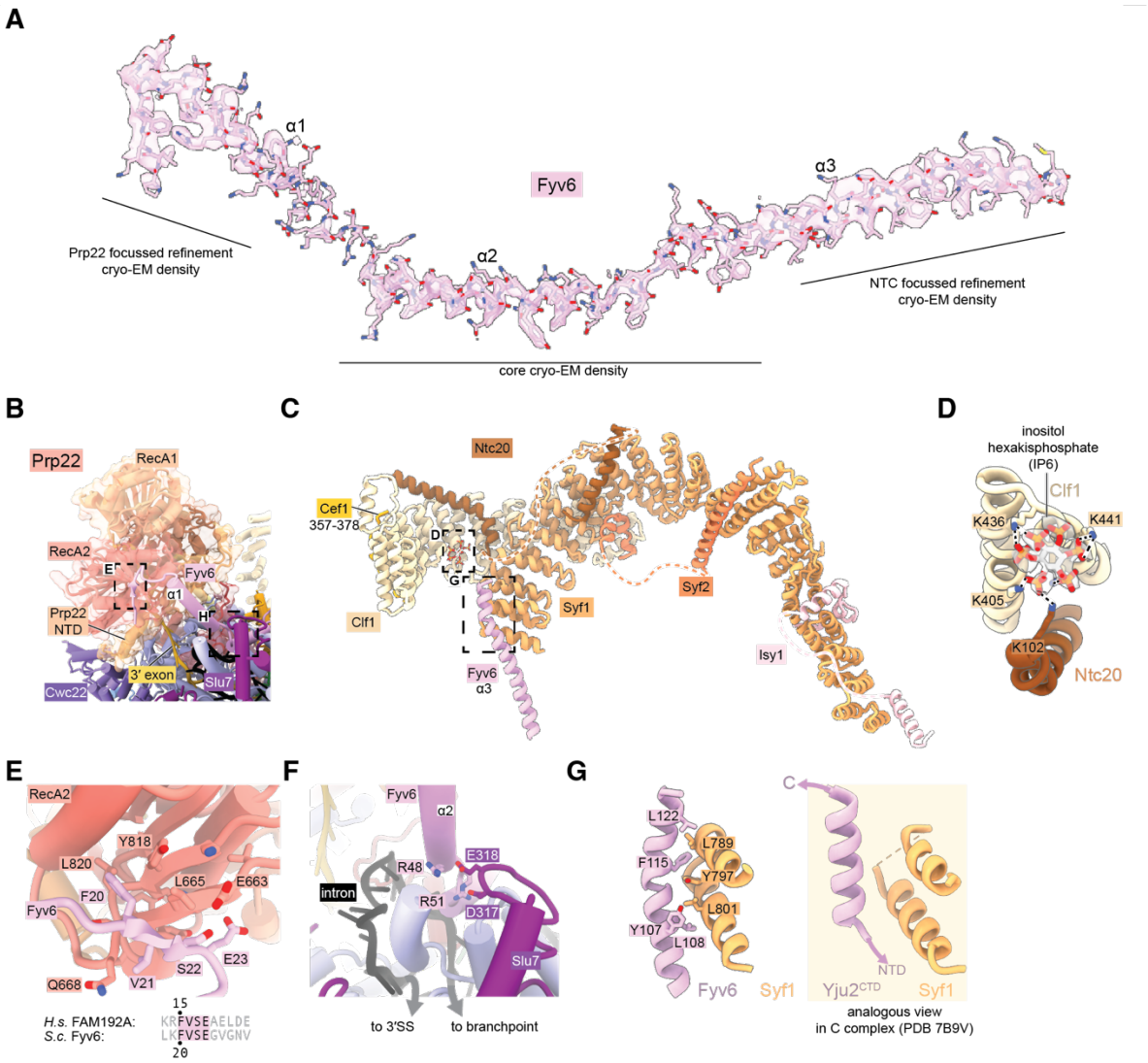

Figure 4. Fyv6 and its interactors in the P complex cryo-EM structure. A) Cryo-EM density segmented around Fyv6. **B)** Structure of Prp22. **C)** Structure of the NTC within P complex. **D)** IP_6 site and cryo-EM density in NTC. **E)** Interaction of the hook domain of Fyv6 with the Prp22 RecA2 domain. **F)** Interaction of Fyv6 with Slu7 and the region of the intron between the BP and 3' SS. **G)** Interaction of Fyv6 with Syf1 and an analogous view of the interaction of Syf1 with Yju2 in C complex (Wilkinson et al., 2021).

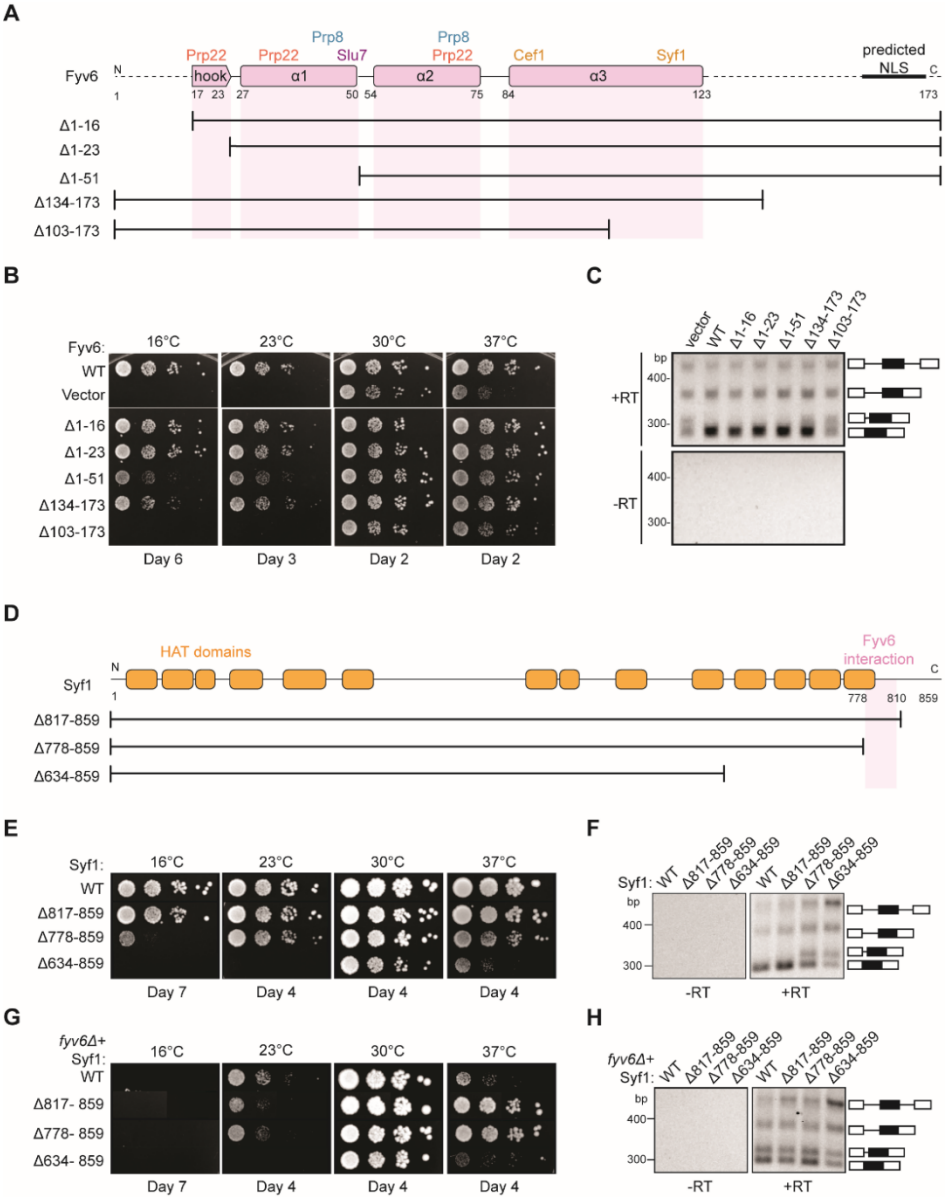

Figure 5. Structure-based analysis of Fyv6 domain function. A) Diagram of Fyv6 protein structure, protein interactors, and protein truncations. NLS= nuclear localization signal **B)** Spot dilution assay of strains with Fyv6 truncations on –Trp DO plates at different temperatures. Plates were imaged after the number of days indicated. **C)** Representative gel image of *SUS1* RT-PCR in strains with an empty vector or expressing the indicated Fyv6 variant. (+RT reactions contain reverse transcriptase; -RT control reactions do not contain reverse transcriptase.) **D)** Diagram of Syf1 protein structure and truncations. **E)** Spot dilution assay of strains with Syf1 truncations on –Trp DO plates at different temperatures. Plates were imaged after the number of days indicated. **F)** Representative gel image of *SUS1* RT-PCR in strains with an empty vector or expressing the indicated Syf1 variant. **G)** Temperature growth assay of strains with Syf1 truncations in a *fyv6Δ* background on YPD plates. Plates were imaged after the number of days indicated. **H)** Representative gel image of RT-PCR of *SUS1* in strains with plasmids containing WT Syf1 or a Syf1 truncation in a *fyv6Δ* background.

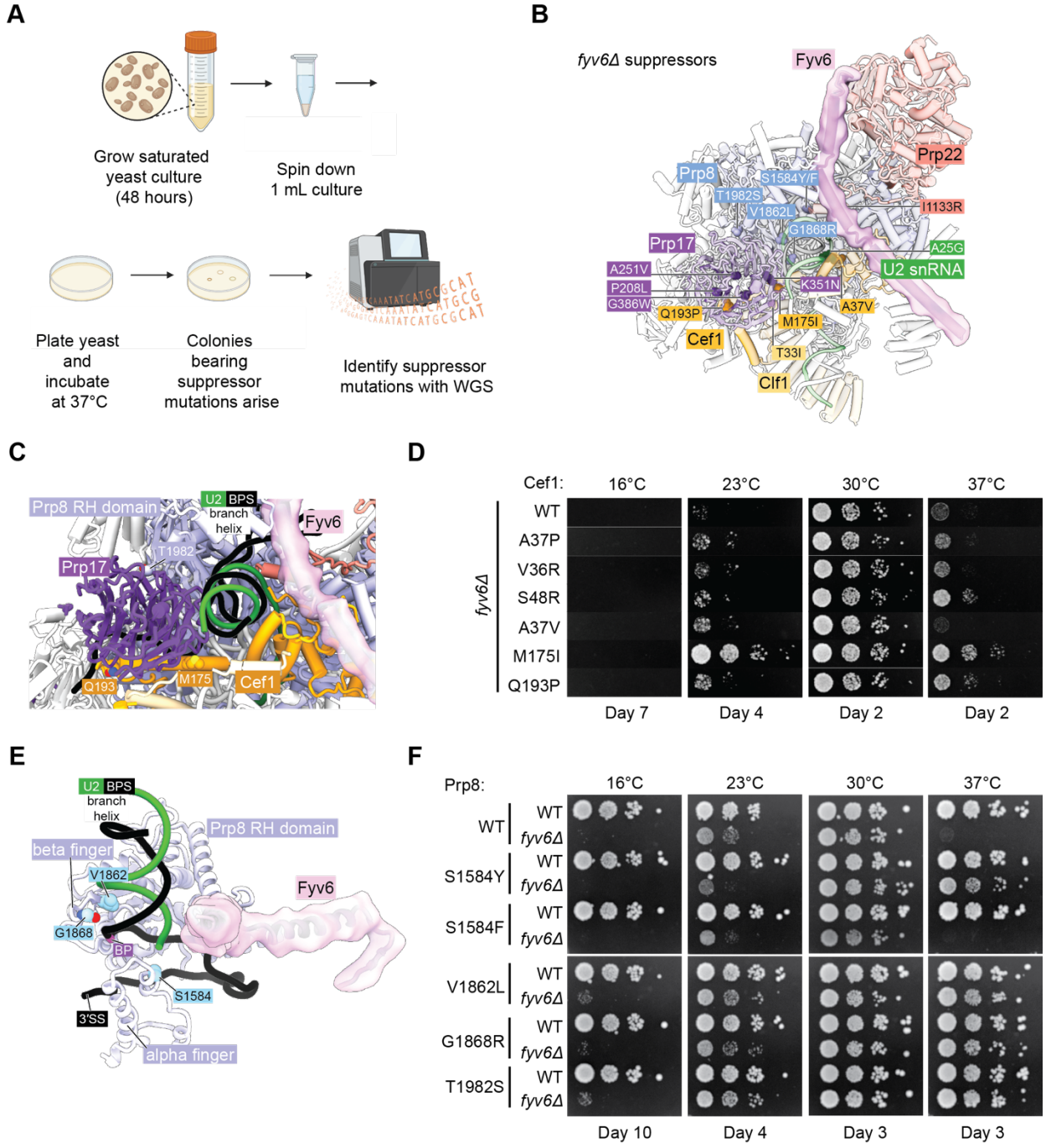

Figure 6. Identification of novel suppressors of *fyv6Δ* temperature sensitivity. A) Workflow for the suppressor screen. **B)** P complex spliceosome structure with *fyv6Δ* suppressor mutations labelled. (See **Supplemental Table S5**) **C)** Close-up view of Cef1 and Prp8 suppressor mutations in P complex. **D)** Spot dilution temperature growth assay with Cef1 mutants on YPD plates. Plates were imaged after the number of days indicated. **E)** Close-up view of Prp8 mutations in P complex. **F)** Spot dilution temperature growth assay with Prp8 mutants on YPD plates. Plates were imaged after the number of days indicated.

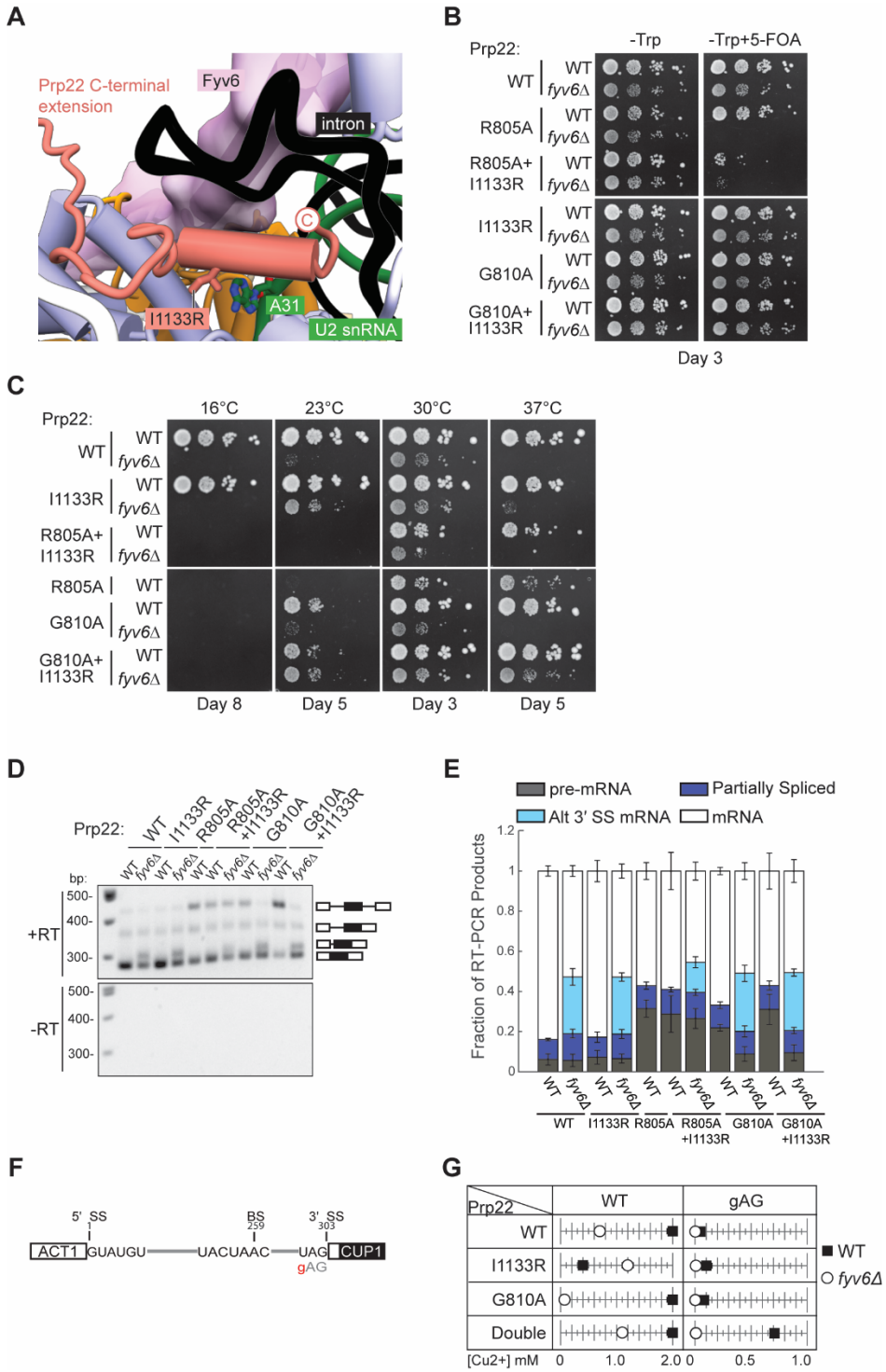

Figure 7. Genetic interactions between Prp22 and Fyv6. A) Location of the Prp22 I1133R *fyv6Δ* suppressor in the P complex structure. **B)** Spot dilution growth assay with Prp22 mutants in WT or *fyv6Δ* backgrounds grown on –Trp DO or –Trp+5-FOA plates. Plates were imaged after 3 days at 30°C. **C)** Spot dilution growth assay with strains containing Prp22 mutants on YPD plates at different temperatures. Plates were imaged after the number of days indicated. **D)** Representative gel of *SUS1* RT-PCR products in strains with Prp22 mutants in the presence or

absence of Fyv6. **E)** Quantitation of band intensities for each *SUS1* splice isoform as a fraction of total product in the lane. Bars indicate average ± SD of *N*=3 replicates. **F)** ACT1-CUP1 reporter construct with the location of the 3' SS substitution noted. **G)** Copper tolerance for each ACT1-CUP1 reporter with each Prp22 allele in strains with (■) or without (○) Fyv6 present. Shown is a representative, single replicate of *N*=3.

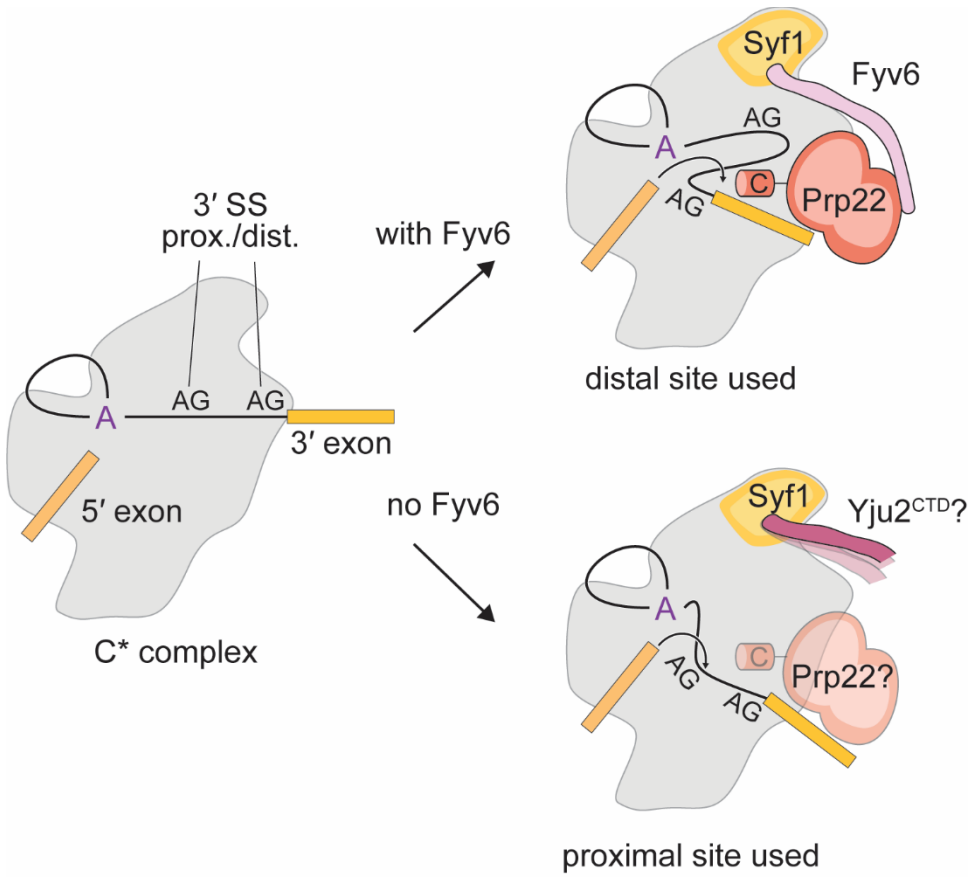

Figure 8. Model for the role of Fyv6 during the 2nd step. Fyv6 interacts with Syf1 and Prp22 and promotes usage of BP distal 3' SS. When Fyv6 is absent, BP proximal 3' SS are favored. It is possible that lack of Fyv6 also results in the presence of Yju2 during exon ligation and relaxing of the requirement for Prp22 at this step.